Post-Print

This is the accepted version of:

X. Wang, M. Morandini, P. Masarati
Modeling and Control for Rotating Pretwisted Thin-Walled Beams with Piezo-Composite
Composite Structures, Vol. 180, 2017, p. 647-663
doi:10.1016/j.compstruct.2017.08.041

Modeling and control for rotating pretwisted thin-walled beams with piezo-composite

Xiao Wang, Marco Morandini, Pierangelo Masarati

Dipartimento di Scienze e Tecnologie Aerospaziali, Politecnico di Milano, Via LaMasa 34, 20156 Milano, Italy

Abstract

In this paper, a rotating thin-walled beam theory incorporating fiber-reinforced and piezo-composite is developed and used to study the active control for vibration suppression. The structural model accounts for transverse shear strain, primary and secondary warpings, pretwist and presetting angles. In addition, the centrifugal stiffening effect, tennis-racket effect, flapping-lagging-transverse shear and extension-twist couplings are accounted as well. Based on a negative velocity feedback control algorithm, the effective damping performance is optimized by studying anisotropic characteristics of piezo-actuators and elastic tailoring of the host structure. Moreover, relations between damping control authority and design factors, such as rotor speed, presetting and pretwist angles are investigated in detailed.

Keywords: rotary thin-walled beam, fiber-reinforced, piezocompsoite, dynamical control

Nomenclature

a_{ij}	1-D global stiffness coefficients
$\mathcal{A}_i^X$	piezo-actuator coefficients, see Eq. 22
b_w	bimomnt of the external force per unit span
b_{ij}	inertial coefficients
$2b$, $2d$	width and depth of the beam cross-section, see Fig. 2
B_w	bimoment

F_w, $a(s)$	primary and secondary warping function, respectively
k_i	control gains in the velocity feedback control in Eqs. 39 and 40
L	length of the beam, see Fig. 2
m_x, m_y, m_z	external moments per unit span, about $x-$, $y-$ and $z-$axes, respectively
M_x, M_z	bending moments about x and z axes, respectively
M_y	torque about y axis
N_{hp}, N_h, N_p	numbers of all layers, host layers and piezo-composite layers, respectively
p_x, p_y, p_z	external forces per unit span
$P(y)$	distribution function along span for the actuator
$\bar{Q}_{ij}$	reduced elastic coefficients
Q_x, Q_z	transverse shear forces in the $x-$ and $z-$directions
R_0	radius of the hub, see Fig. 2
$\mathbf{R}$	position vector of a point on the deformed beam, see Eq. 3
(s, y, n)	local coordinate system on the cross-section, see Fig. 2
T_y	axial force in the $y-$direction
u_0, v_0, w_0	displacement components of the cross-section along x, y, z axes, see Fig. 2
V_i	voltage parameters, see Eqs. 23
(x, y, z)	rotating axis system located at the blade root, see Fig. 1
(x^p, y^p, z^p)	local coordinate system for an arbitrary beam cross-section, see Fig. 2.
(X, Y, Z)	inertial reference system attached to the center of hub
$\beta(y)$	pretwist angle, see Eq. 2
β_0, γ_0	pretwist angle at beam tip and presetting angle at beam root, respectively
$\rho_{(k)}$	mass density of the kth layer in Eq. 15a
Γ_t	nonlinear force related to twist motion
θ_h, θ_p	ply-angles of host structure and piezo-actuator
θ_x, ϕ, θ_z	rotations of the cross-section about the x, y and z axes, see Fig. 2
Ω	rotating speed of hub
δ	variation operator
δ_p, δ_s	tracers that take the value 1 or 0
$\dot{()}$, $\ddot{()}$,$()'$, $()''$	$\partial()/\partial t$, $\partial^2()/\partial t^2$, $\partial()/\partial y$, $\partial^2()/\partial y^2$

$\mathbf{X}^T$	transpose of the matrix or vector $\mathbf{X}$
$\oint_c$, $\int_0^L$	integral along the cross-section and the span, respectively

1. Introduction

In recent years a large amount of work are devoted to the modeling and behavior of composite rotor blades [1, 2, 3, 4, 5]. Among there works, Rehfield et al. [6] discussed the non-classic behavior of a closed cross-section composite thin-walled beam. Chandra et al. [7] investigated the vibration characteristics of rotating composite box beams on both experimental and theoretical aspects. Song et al [8, 9] developed a rotating composite thin-walled beam theory feathering lateral bending-vertical bending elastic coupling effect. Oh et al discussed effects of pretwist and presetting on coupled bending vibrations [10]. He also investigated the twist-extension elastic coupling effect on rotary composite structure [11].

Rotor blades operate in a unsteady and complex aerodynamic environment. They are also characterized by a complex structural behavior. For these reasons active control is deemed to te a promising technology for the design of new high performing blades [12, 13]. Because piezoelectric materials have a series of desirable characteristics, such as self-sensing, structure embeddability, fast response and covering a broad range of frequency, they are often proposed for the design of active blades [14, 15, 16]. In order to overcome the drawbacks of the typical piezoceramic actuator, such as the vulnerable ability to damage and the fact that they can hardly conform to a curved surface, piezo-composite actuators, e.g., Active Fiber Composite (AFC) [17] and Macro-Fiber Composite (MFC) [18] were developed. In the existing literatures, a lot publications on modeling or studying adaptive thin-walled structure are based on a piezoelectric bending moment control system [19, 20, 21, 22, 23, 24], but they lack explicit discussions for transverse shear force and twist moment actuations. Thus a comprehensive study allowing to get a better insight into the influence of piezoelectric extension, transverse shear, twist, bimoment and bending actuations on rotary thin-walled structures is still interesting.

In this paper, a geometrically nonlinear rotating thin-walled beam theory incorporating piezo-composite is developed. In addition, transverse shear strain, primary and secondary warping inhibitions, three-dimensional strain, centrifugal stiffening and tennis-racket effects [25] are taken into account. The circumferentially uniform stiffness (CUS) [26] lay-up configuration that yields lateral bending-vertical bending and twist-extension couplings is applied for the rotary structure [11, 27, 28]. The governing equations and the boundary conditions are derived via Hamilton's principle. Numerical studies are based on the Extended Galerkin's Method. Based on a negative velocity feedback control methodology, active control for vibration suppression is optimized via the study of tailoring technology and anisotropic characteristic of piezo-composite. In addition, the influences of design parameters, such as rotor speed, presetting and pretwist angles are investigated, and pertinent conclusions are outlined.

2. Basic assumptions and kinematics

2.1. Basic assumptions

The geometric configuration and the chosen coordinate systems of the rotary thin-walled beam are shown in Figs 1 and 2. The inertial reference system (X, Y, Z) is attached to the center of the hub O (considered to be rigid), while the rotating axis system (x, y, z) is located at the blade root with an offset R_0 from the rotation axis O, see Fig. 1. The unit vectors associated with the frame coordinates (X, Y, Z) and (x, y, z) are defined as $(\mathbf{I}, \mathbf{J}, \mathbf{K})$ and $(\mathbf{i}, \mathbf{j}, \mathbf{k})$, respectively. Besides the rotating coordinate system (x, y, z), a local coordinate system (x^p, y, z^p) is also defined, where x^p and z^p are the principal axes of an arbitrary beam cross-section, see Fig. 2. In addition, a surface coordinate system (s, y, n) on the mid-line contour of the cross-section is considered in Fig. 2. Coordinate systems (x, y, z) and (x^p, y, z^p) are related by the following

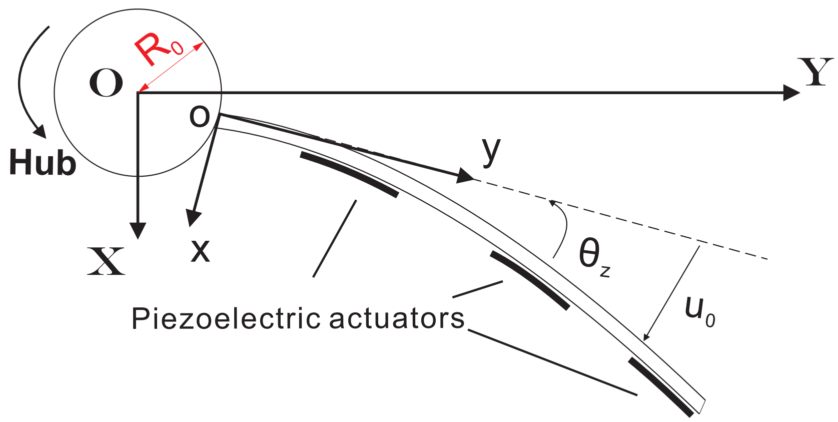

Figure 1: A schematic description of the blade.

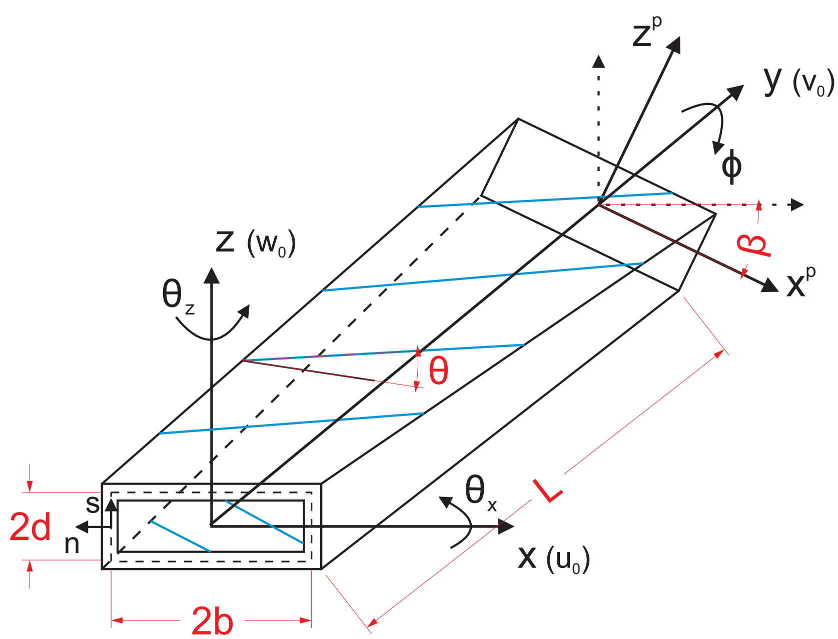

Figure 2: Geometry of the pretwisted beam with a rectangular cross-section (CUS lay-ups).

transformation

$$\begin{cases} x(s,y) = x^p(s)\cos\beta(y) + z^p(s)\sin\beta(y), \\ z(s,y) = -x^p(s)\sin\beta(y) + z^p(s)\cos\beta(y), \end{cases} \tag{1}$$

where the linear pretwist angle $\beta(y)$ can be assumed as

$$\beta(y) = \gamma_0 + \beta_0 y/L, \tag{2}$$

in which γ_0, β_0 and L denote the presetting angle, the pretwist angle of the cross-section at the beam tip and the length of the beam, respectively.

The rotary thin-walled structure is modeled assuming that the cross-section is preserved during the deformation. Beside this assumption, already adopted e.g. in Ref. [29], no other significant assumptions to the kinematic description are introduced; in particular, both the primary and secondary (thickness) warping effects are included and the transverse shear effect are taken into account. Note also that the centrifugal stiffening and tennis-racket effects [25] are accounted for in the present approach.

2.2. Kinematics

It is useful to express the position vector $\mathbf{R}$ of an arbitrary point $M(x,y,z)$ belonging to the deformed beam, measured from a fixed origin O (coinciding with the center of the hub), described in the rotating coordinate system (x,y,z). In the sense we have

$$\mathbf{R} = \mathbf{R}_0 + \mathbf{r} + \mathbf{\Delta}, \tag{3}$$

where $\mathbf{R}_0$, $\mathbf{r}$ and $\mathbf{\Delta}$ denote the position vector of the beam root point o (hub periphery), the undeformed position vector of point $M(x,y,z)$, and its displacement vector, respectively. Their expressions are

$$\mathbf{R}_0 = R_0\mathbf{j}, \quad \mathbf{r} = x\mathbf{i} + y\mathbf{j} + z\mathbf{k}, \quad \mathbf{\Delta} = u\mathbf{i} + v\mathbf{i} + w\mathbf{k}, \tag{4}$$

where the components u, v and w in the displacement vector $\mathbf{\Delta}$ are [29]

$$u(x,y,z,t) = u_0(x,t) + \left[z(s) + n\frac{\mathrm{d}\,x}{\mathrm{d}\,s}\right]\sin\phi(y,t) - \left[x(s) - n\frac{\mathrm{d}\,z}{\mathrm{d}\,s}\right]\left[1 - \cos\phi(y,t)\right], \tag{5a}$$

$$
\begin{aligned}
v(x,y,z,t) = & v_0(y,t) + \left[x(s) - n\frac{\mathrm{d}\,z}{\mathrm{d}\,s}\right]\theta_z(y,t) + \left[z(s) + n\frac{\mathrm{d}\,x}{\mathrm{d}\,s}\right]\theta_x(y,t) \\
& - \left[F_w(s) + na(s)\right]\phi'(y,t),
\end{aligned} \tag{5b}
$$

$$
w(x,y,z,t) = w_0(y,t) - \left[x(s) - n\frac{\mathrm{d}\,z}{\mathrm{d}\,s}\right]\sin\phi(y,t) - \left[z(s) + n\frac{\mathrm{d}\,x}{\mathrm{d}\,s}\right][1 - \cos\phi(y,t)], \tag{5c}
$$

where $F_w(s)$ and $na(s)$ play the role of primary and secondary warping functions. $u_0(y,t)$, $v_0(y,t)$, $w_0(y,t)$, $\phi(y,t)$, $\theta_x(y,t)$, $\theta_z(y,t)$ represent the 1-D displacement measures (see Fig. 2), and constitute the basic unknowns of the problem. If we assume that the rotation takes place in the plane (X,Y) with the constant angular speed, i.e., $\mathbf{\Omega} = \Omega\mathbf{K} = \Omega\mathbf{k}$, the velocity and acceleration vectors of point $M(x,y,z)$ can be given as:

$$
\begin{aligned}
\dot{\mathbf{R}}(x,y,z) = & \dot{u}(x,y,z)\mathbf{i} - [R_0 + y + v(x,y,z)]\Omega\mathbf{i} + \dot{v}(x,y,z)\mathbf{j} \\
& + [x + u(x,y,z)]\Omega\mathbf{j} + \dot{w}\mathbf{k},
\end{aligned} \tag{6}
$$

$$
\begin{aligned}
\ddot{\mathbf{R}}(x,y,z) = & \ddot{u}(x,y,z)\mathbf{i} - 2\dot{v}(x,y,z)\Omega\mathbf{i} - [x + u(x,y,z)]\Omega^2\mathbf{i} + \ddot{v}(x,y,z)\mathbf{j} \\
& + 2\dot{u}(x,y,z)\Omega - [R_0 + y + v(x,y,z)]\Omega^2\mathbf{j} + \ddot{w}\mathbf{k}.
\end{aligned} \tag{7}
$$

3. Constitutive Relations

The fiber-reinforced composite material (e.g. Graphite-Epoxy) in host structure and the piezo-composite material (e.g. AFC or MFC) in actuator can both be modeled using the linear piezoelectric constitutive equation [30, 31]

$$
\begin{Bmatrix} \sigma_{11} \\ \sigma_{22} \\ \sigma_{33} \\ \tau_{23} \\ \tau_{31} \\ \tau_{12} \end{Bmatrix} = \begin{bmatrix} C_{11} & C_{12} & C_{13} & 0 & 0 & 0 \\ C_{12} & C_{22} & C_{23} & 0 & 0 & 0 \\ C_{13} & C_{23} & C_{33} & 0 & 0 & 0 \\ 0 & 0 & 0 & C_{44} & 0 & 0 \\ 0 & 0 & 0 & 0 & C_{55} & 0 \\ 0 & 0 & 0 & 0 & 0 & C_{66} \end{bmatrix} \begin{Bmatrix} \varepsilon_{11} \\ \varepsilon_{22} \\ \varepsilon_{33} \\ \gamma_{23} \\ \gamma_{31} \\ \gamma_{12} \end{Bmatrix} - \begin{Bmatrix} e_{11} \\ e_{12} \\ e_{13} \\ 0 \\ 0 \\ 0 \end{Bmatrix} E_1. \tag{8}
$$

If we assume constant electric filed through the actuator thickness, then $E_1 = -(V/\hat{h})$, where V and $\hat{h}$ are the applied voltage and electrode spacing of the interdigitated electrode for the actuator layer, respectively.

Thus for kth layer, Eq. (8) referred to the surface coordinate system (s, y, n) in Fig. 2 can be reduced to the plane stress condition $\sigma_{nn} = 0$ as

$$\begin{Bmatrix} \sigma_{ss} \\ \sigma_{yy} \\ \tau_{yn} \\ \tau_{sn} \\ \tau_{sy} \end{Bmatrix}_{(k)} = \begin{bmatrix} \bar{Q}_{11} & \bar{Q}_{12} & 0 & 0 & \bar{Q}_{16} \\ \bar{Q}_{12} & \bar{Q}_{22} & 0 & 0 & \bar{Q}_{26} \\ 0 & 0 & \bar{Q}_{44} & \bar{Q}_{45} & 0 \\ 0 & 0 & \bar{Q}_{45} & \bar{Q}_{55} & 0 \\ \bar{Q}_{16} & \bar{Q}_{26} & 0 & 0 & \bar{Q}_{66} \end{bmatrix}_{(k)} \begin{Bmatrix} \varepsilon_{ss} \\ \varepsilon_{yy} \\ \gamma_{yn} \\ \gamma_{sn} \\ \gamma_{sz} \end{Bmatrix}_{(k)} - \begin{Bmatrix} e_{ss} \\ e_{yy} \\ 0 \\ 0 \\ e_{sy} \end{Bmatrix}_{(k)} E_{1(k)}, \tag{9}$$

in which the expressions of reduced elastic coefficients $\bar{Q}_{ij}$ and reduced piezo-electric stress coefficients e_{ss}, e_{yy}, e_{sy} can be found in Refs. [31, p. 575] and [32], respectively.

Based on the assumption that the stress resultants N_{ss} and N_{sn} are negligibly small when compared with the remaining ones [29, 33], the stress resultants and stress couples reduce to the following expressions

$$\begin{Bmatrix} N_{yy} \\ N_{ys} \\ L_{yy} \\ L_{sy} \end{Bmatrix} = \begin{bmatrix} K_{11} & K_{12} & K_{13} & K_{14} \\ K_{21} & K_{22} & K_{23} & K_{24} \\ K_{41} & K_{42} & K_{43} & K_{44} \\ K_{51} & K_{52} & K_{53} & K_{54} \end{bmatrix} \begin{Bmatrix} \epsilon_{yy}^0 \\ \gamma_{ys}^0 \\ \phi' \\ \epsilon_{yy}^1 \end{Bmatrix} - \begin{Bmatrix} \tilde{N}_{yy} \\ \tilde{N}_{sy} \\ \tilde{L}_{yy} \\ \tilde{L}_{sy} \end{Bmatrix}, \tag{10}$$

and

$$N_{yn} = \left(A_{44} - \frac{{A_{45}}^2}{A_{55}} \right) \gamma_{yn}. \tag{11}$$

The explicit expressions of the local stiffness coefficients K_{ij} and the associated strains $(\epsilon_{yy}^0, \epsilon_{yy}^1, \gamma_{ys}^0, \gamma_{yn})$ can be found in Ref. [29]. As for the piezo-actuator induced stress resultant($\tilde{N}_{yy}$, $\tilde{N}_{sy}$) and stress couple ($\tilde{L}_{yy}$, $\tilde{L}_{sy}$), they are defined as

$$
\begin{cases}
\tilde{N}_{yy}(s,y) = \sum_{k=1}^{m} \left(e_{yy} - \dfrac{A_{12}}{A_{11}} e_{ss}\right) E_{1(k)}(n_{k2} - n_{k1}) P_k(s) P_k(y) \\
\tilde{N}_{sy}(s,y) = \sum_{k=1}^{m} \left(e_{sy} - \dfrac{A_{16}}{A_{11}} e_{ss}\right) E_{1(k)}(n_{k2} - n_{k1}) P_k(s) P_k(y) \\
\tilde{L}_{yy}(s,y) = \sum_{k=1}^{m} \left[\dfrac{1}{2} e_{yy}(n_{k1} + n_{k2}) - \dfrac{B_{12}}{A_{11}} e_{ss}\right] E_{1(k)}(n_{k2} - n_{k1}) P_k(s) P_k(y) \\
\tilde{L}_{sy}(s,y) = \sum_{k=1}^{m} \left[\dfrac{1}{2} e_{sy}(n_{k1} + n_{k2}) - \dfrac{B_{16}}{A_{11}} e_{ss}\right] E_{1(k)}(n_{k2} - n_{k1}) P_k(s) P_k(y),
\end{cases}
\tag{12}
$$

where A_{ij} and B_{ij} are the standard local stiffness quantities [30] based on the total number of constituent layers $N_{hp} = N_h + N_p$, for the host layers (N_h) and piezo-composite (N_p). The actuator distribution function $P(\cdot)$ are given as (see Fig. 3)

$$P_k(n) = H(n - n_{k1}) - H(n - n_{k2}), \tag{13a}$$

$$P_k(s) = H(s - s_{k1}) - H(s - s_{k2}), \tag{13b}$$

$$P_k(y) = H(y - y_{k1}) - H(y - y_{k2}), \tag{13c}$$

in which $H(\cdot)$ denotes Heaviside's distribution.

4. Formulation of the governing system

The governing equations and the associated boundary conditions are derived from Hamilton's principle. This can be stated as (see e.g. Ref. [29])

$$\delta J = \int_{t_0}^{t_1} [\delta T + \delta V - \delta W_e]\, \mathrm{d}\, t = 0, \tag{14}$$

where t_0 and t_1 denote two arbitrary motions of time; W_e denotes the virtual work of the external forces; and the kinetic energy T and strain energy V can be given as

$$T = \frac{1}{2} \int_0^L \oint_c \sum_{k=1}^{N_{hp}} \int_{n_{k1}}^{n_{k2}} \rho\,(k) (\dot{\mathbf{R}} \cdot \dot{\mathbf{R}})\, \mathrm{d}\, n\, \mathrm{d}\, s\, \mathrm{d}\, y, \tag{15a}$$

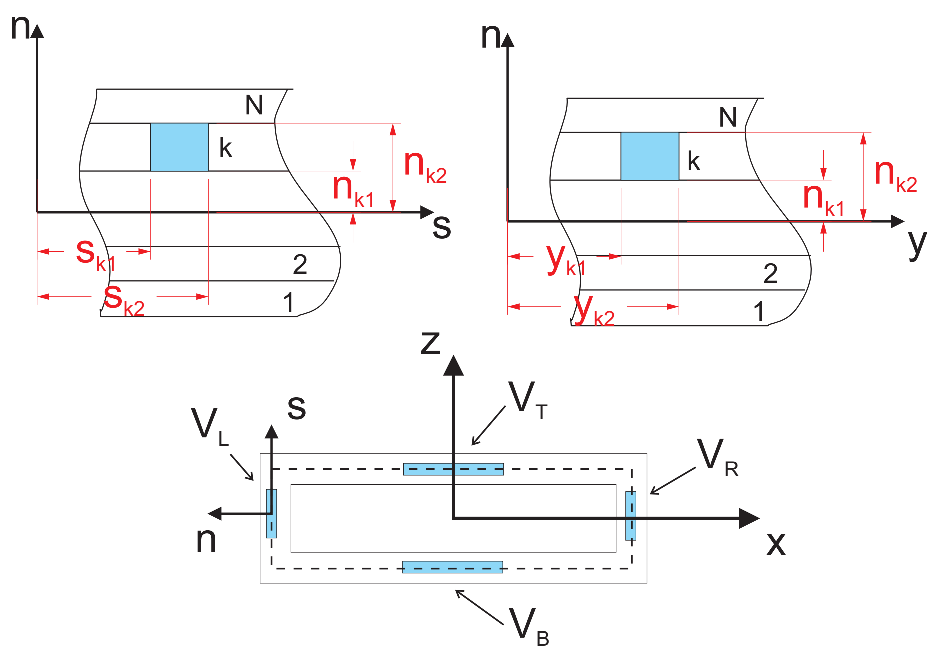

Figure 3: Piezo-actuator location.

$$V = \frac{1}{2}\int_0^L \oint_c \Big[N_{yy}\varepsilon_{yy}^0 + N_{ys}\gamma_{sy}^0 + L_{yy}\varepsilon_{yy}^1 + L_{sy}\phi' + N_{ny}\gamma_{ny}\Big]\,\mathrm{d}\,s\,\mathrm{d}\,y. \tag{15b}$$

After a lengthy variation process and collecting the terms associated with the same variations, the governing equations can be obtained,

$$\begin{aligned}\delta u_0 : &[(T_y + \tilde{T}_y)u_0' - (M_z + \tilde{M}_z)\phi' \sin\phi + (M_x + \tilde{M}_x)\phi' \cos\phi + (Q_x + \tilde{Q}_x)\cos\phi \\ &+ (Q_z + \tilde{Q}_z)\sin\phi]' + p_x - b_1[\ddot{u}_0 - \utilde{2\Omega\dot{v}_0} - \underline{\Omega^2 u_0}] = 0,\end{aligned} \tag{16a}$$

$$\delta v_0 : \ (T_y + \tilde{T}_y)' + p_y - b_1[\ddot{v}_0 + \utilde{2\Omega\dot{u}_0} - \underline{\Omega^2(R_0 + y + v_0)}] = 0, \tag{16b}$$

$$\begin{aligned}\delta w_0 : &[(T_y + \tilde{T}_y)w_0' - (M_z + \tilde{M}_z)\phi' \cos\phi - (M_x + \tilde{M}_x)\phi' \sin\phi \\ &- (Q_x + \tilde{Q}_x)\sin\phi + (Q_z + \tilde{Q}_z)\cos\phi]' + p_z - b_1\ddot{w}_0 = 0,\end{aligned} \tag{16c}$$

$$
\begin{aligned}
\delta\phi : &(M_y + \tilde{M}_y)' - (B_w + \tilde{B}_w)'' + [(M_x + \tilde{M}_x)(u_0' \cos\phi - w_0' \sin\phi) \\
&- (M_z + \tilde{M}_z)(w_0' \cos\phi + u_0' \sin\phi) + (\Gamma_t + \tilde{\Gamma}_t)\phi']' \\
&+ (M_x + \tilde{M}_x)(u_0'\phi' \sin\phi + w_0'\phi' \cos\phi) - (M_z + \tilde{M}_z)(w_0'\phi' \sin\phi - u_0'\phi' \cos\phi) \\
&+ (Q_x + \tilde{Q}_x)(u_0' \sin\phi + w_0' \cos\phi) - (Q_z + \tilde{Q}_z)(u_0' \cos\phi - w_0' \sin\phi) \\
&+ m_y + b_w' - (b_4 + b_5)\ddot{\phi} + 2\Omega\left[(b_4 \cos\phi - b_6 \sin\phi)\dot{\theta}_x + (b_6 \cos\phi - b_5 \sin\phi)\dot{\theta}_z\right] \\
&+ \Omega^2\left[(b_4 - b_5)\sin\phi\cos\phi + b_6\cos\phi(\cos\phi - \sin\phi)\right] + b_{10}(\ddot{\phi}'' - \Omega^2\phi'') = 0,
\end{aligned}
\tag{16d}
$$

$$
\begin{aligned}
\delta\theta_x : &(M_x + \tilde{M}_x)' - (Q_z + \tilde{Q}_z) + m_x - b_4\ddot{\theta}_x - b_6\ddot{\theta}_z \\
&- 2\Omega(b_4 \cos\phi - b_6 \sin\phi)\dot{\phi} + \Omega^2(b_4\theta_x + b_6\theta_z) = 0,
\end{aligned}
\tag{16e}
$$

$$
\begin{aligned}
\delta\theta_z : &(M_z + \tilde{M}_z)' - (Q_x + \tilde{Q}_x) + m_z - b_5\ddot{\theta}_z - b_6\ddot{\theta}_x \\
&- 2\Omega(b_6 \cos\phi - b_5 \sin\phi)\dot{\phi} + \Omega^2(b_5\theta_z + b_6\theta_x) = 0,
\end{aligned}
\tag{16f}
$$

and the essential boundary conditions at $y = 0$ are

$$
u_0 = v_0 = w_0 = \phi = \phi' = \theta_x = \theta_z = 0,
\tag{17}
$$

the natural boundary conditions at $y = L$ are

$$
\delta u_0 \ : T_y u_0' - M_z\phi' \sin\phi + M_x\phi' \cos\phi + Q_x \cos\phi + Q_z \sin\phi = \bar{Q}_x,
\tag{18a}
$$

$$
\delta v_0 \ : \ T_y = \bar{T}_y,
\tag{18b}
$$

$$
\delta w_0 \ : T_y w_0' - M_z\phi' \cos\phi - M_x\phi' \sin\phi - Q_x \sin\phi + Q_z \cos\phi = \bar{Q}_z,
\tag{18c}
$$

$$
\begin{aligned}
\delta\phi \ : \ &- B_w' + M_y + M_x(u_0' \cos\phi - w_0' \sin\phi) \\
&- M_z(w_0' \cos\phi + u_0' \sin\phi) + \Gamma_t\phi' + \Gamma_t\phi' + b_{10}(\ddot{\phi}' - \Omega^2\phi') = \bar{M}_y,
\end{aligned}
\tag{18d}
$$

$$\delta\phi' \ : \ B_w = \bar{B}_w, \tag{18e}$$

$$\delta\theta_x \ : \qquad M_x = \bar{M}_x, \tag{18f}$$

$$\delta\theta_z \ : \ M_z = \bar{M}_z. \tag{18g}$$

In these equations, the terms associated with (1) the centrifugal acceleration, (2) the Coriolis, (3) the tennis-racket, (4) the centrifugal warping and (5) the centrifugal-rotatory effects are underscored by (1) a solid line ($\underline{\qquad}$), (2) a wavy line ($\underset{\sim\sim\sim}{\qquad}$), (3) a dotted line ($\underset{....}{\quad}$), (4) a dashed line ($\underset{---}{\quad}$) and (5) two superposed solid lines ($\underline{\underline{\qquad}}$) respectively. More details about these high rotating speed induced effects can be found e.g. in Refs. [31, 25, 8]. The inertial coefficients b_{ij} are defined in Appendix A; p_x, p_y, p_z and m_x, m_y, m_z are the external forces and moments per unit span, respectively; b_w is the external bimoment of the surface traction. As for the 1-D stress resultants, T_y is the axial force, Q_x the transverse shear force in the $x-$direction, Q_z the transverse shear force in the $z-$direction; M_x the bending moment around $x-$axis, M_y the torque, M_z the bending moment around $z-$axis, B_w the bimoment. The nonlinear stress couple is Γ_t. Terms without and with over-tilde ($\tilde{\ }$) identify the pure mechanical and piezo-actuator contributions, respectively. The terms with over-bar ($\bar{\ }$) are external excitations on the beam tip. Their explicit expressions will be discussed in the following section.

5. Governing equations for circumferentially uniform stiffness lay-up configuration

A special structural configuration, viz., *circumferentially uniform stiffness* (CUS) configuration was firstly proposed by Rehfield and Atilgan [34] and is considered here. For the thin-walled beam with rectangular cross-section as shown in Fig. 2, a CUS configuration implies the ply-angle distribution $\theta(z) =$

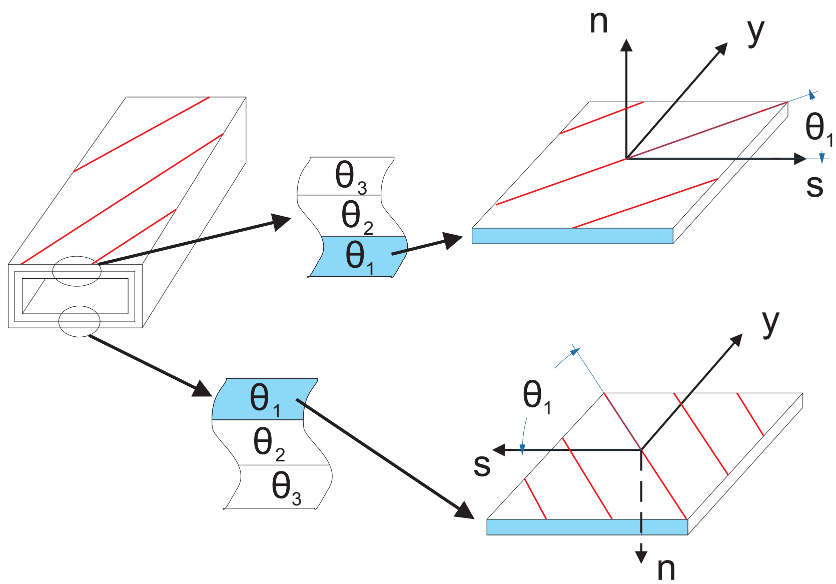

Figure 4: Circumferentially uniform stiffness (CUS) configuration

$\theta(-z)$ of the top and bottom walls and $\theta(x) = \theta(-x)$ of the left and right walls, see Fig. 4.

5.1. Force-displacement relationship

The expressions of pure mechanical stress resultants and stress couples in Eqs. (16) and (18) can be written as [29]:

$$\left\{\begin{array}{c} T_y \\ M_z \\ M_x \\ Q_x \\ Q_z \\ B_w \\ M_y \\ \Gamma_t \end{array}\right\} = [a_{ij}(y)] \left\{\begin{array}{c} v_0' + \frac{1}{2}(u_0')^2 + \frac{1}{2}(w_0')^2 \\ \theta_z' - w_0'\phi'\cos\phi - u_0'\phi'\sin\phi \\ \theta_x' + u_0'\phi'\cos\phi - w_0'\phi'\sin\phi \\ \theta_z + u_0'\cos\phi - w_0'\sin\phi \\ \theta_x + u_0'\sin\phi + w_0'\cos\phi \\ \phi'' \\ \phi' \\ \frac{1}{2}(\phi')^2 \end{array}\right\}, \tag{19}$$

in which the global stiffness quantities $a_{ij}(y)$ can be expressed in local stiffness quantities a_{ij}^p, the details are given in Appendix B. For a general anisotropic material, the stiffness matrix $[a_{ij}(y)]$ is fully populated, implying all motions (flapping, lagging, twist) are coupled. However, applying circumferentially uniform stiffness (CUS) lay-up configuration will yield $[a_{ij}(y)]$ decoupling into two, viz, extension-twist coupling,

$$\begin{Bmatrix} T_y \\ M_y \\ B_w \\ \Gamma_t \end{Bmatrix} = \begin{bmatrix} a_{11} & a_{17} & 0 & a_{18} \\ a_{17} & a_{77} & 0 & a_{78} \\ 0 & 0 & a_{66} & 0 \\ a_{18} & a_{78} & 0 & a_{88} \end{bmatrix} \begin{Bmatrix} v_0' + \dfrac{1}{2}(u_0')^2 + \dfrac{1}{2}(w_0')^2 \\ \phi' \\ \phi'' \\ \dfrac{1}{2}(\phi')^2 \end{Bmatrix}, \tag{20}$$

and bending-transverse shear coupling,

$$\begin{Bmatrix} M_z \\ M_x \\ Q_x \\ Q_z \end{Bmatrix} = \begin{bmatrix} a_{22}(y) & a_{23}(y) & a_{24}(y) & a_{25}(y) \\ a_{23}(y) & a_{33}(y) & a_{34}(y) & a_{35}(y) \\ a_{24}(y) & a_{34}(y) & a_{44}(y) & a_{45}(y) \\ a_{25}(y) & a_{35}(y) & a_{45}(y) & a_{55}(y) \end{bmatrix} \begin{Bmatrix} \theta_z' - w_0'\phi'\cos\phi - u_0'\phi'\sin\phi \\ \theta_x' + u_0'\phi'\cos\phi - w_0'\phi'\sin\phi \\ \theta_z + u_0'\cos\phi - w_0'\sin\phi \\ \theta_x + u_0'\sin\phi + w_0'\cos\phi \end{Bmatrix}. \tag{21}$$

Note that, a_{ij} in Eq. (20) are independent of spanwise coordinate, i.e., $a_{ij}(y) = a_{ij}^p$. While in Eq. (21), a_{23}^p, a_{24}^p, a_{35}^p and a_{45}^p, these four local stiffness quantities are all zero in the expressions of $a_{ij}(y)$.

5.2. *Force-voltage relationship*

The relation between stress resultants, couples induced by piezo-actuators and applied voltages described in the local coordinate system (x^p, y, z^p) can be given as

$$\begin{Bmatrix} \tilde{T}_y(y,t) \\ \tilde{M}_y(y,t) \\ \tilde{B}_w(y,t) \\ \tilde{\Gamma}_t(y,t) \\ \tilde{M}_z(y,t) \\ \tilde{M}_x(y,t) \\ \tilde{Q}_x(y,t) \\ \tilde{Q}_z(y,t) \end{Bmatrix} = \begin{bmatrix} \mathcal{A}_1^{Ty} & \mathcal{A}_2^{Ty} & \mathcal{A}_3^{Ty} & \mathcal{A}_4^{Ty} \\ \mathcal{A}_1^{My} & \mathcal{A}_2^{My} & \mathcal{A}_3^{My} & \mathcal{A}_4^{My} \\ \mathcal{A}_1^{Bw} & \mathcal{A}_2^{Bw} & \mathcal{A}_3^{Bw} & \mathcal{A}_4^{Bw} \\ \mathcal{A}_1^{\Gamma t} & \mathcal{A}_2^{\Gamma t} & \mathcal{A}_3^{\Gamma t} & \mathcal{A}_4^{\Gamma t} \\ \mathcal{A}_1^{Mz} & \mathcal{A}_2^{Mz} & \mathcal{A}_3^{Mz} & \mathcal{A}_4^{Mz} \\ \mathcal{A}_1^{Mx} & \mathcal{A}_2^{Mx} & \mathcal{A}_3^{Mx} & \mathcal{A}_4^{Mx} \\ \mathcal{A}_1^{Qx} & \mathcal{A}_2^{Qx} & \mathcal{A}_3^{Qx} & \mathcal{A}_4^{Qx} \\ \mathcal{A}_1^{Qz} & \mathcal{A}_2^{Qz} & \mathcal{A}_3^{Qz} & \mathcal{A}_4^{Qz} \end{bmatrix} \begin{Bmatrix} V_1(t) \\ V_2(t) \\ V_3(t) \\ V_4(t) \end{Bmatrix} P(y), \tag{22}$$

where $P(y)$ of Eq. (13c) denotes the span location of the piezo-actuator. The local piezo-actuator coefficients $\mathcal{A}_i^X$ $(i = 1, 2, 3, 4)$ are defined in Appendix C. The voltage parameters V_i $(i = 1, 2, 3, 4)$ are defined as

$$V_1(t) = \frac{1}{2}\left[V_T(t) - V_B(t)\right], \quad V_2(t) = \frac{1}{2}\left[V_T(t) + V_B(t)\right], \tag{23a}$$

$$V_3(t) = \frac{1}{2}\left[V_L(t) - V_R(t)\right], \quad V_4(t) = \frac{1}{2}\left[V_L(t) + V_R(t)\right], \tag{23b}$$

in which four voltage parameters V_T, V_B, V_L and V_R denote voltages applied on actuators located at the top, bottom, left and right plates of the beam, see Fig. 3. Applying CUS lay-up configuration and described in the rotating coordinate system (x, y, z), Eq. (22) will be reduced as two actuating groups, viz., extension-twist actuating coupling

$$\begin{Bmatrix} \tilde{T}_y(y,t) \\ \tilde{M}_y(y,t) \\ \tilde{B}_w(y,t) \\ \tilde{\Gamma}_t(y,t) \end{Bmatrix} = \begin{bmatrix} \mathcal{A}_2^{Ty} & \mathcal{A}_4^{Ty} \\ \mathcal{A}_2^{My} & \mathcal{A}_4^{My} \\ 0 & 0 \\ \mathcal{A}_2^{\Gamma t} & \mathcal{A}_4^{\Gamma t} \end{bmatrix} \begin{Bmatrix} V_2(t) \\ V_4(t) \end{Bmatrix} P(y), \tag{24}$$

and bending-transverse shear actuating coupling

$$\begin{Bmatrix} \tilde{M}_z(y,t) \\ \tilde{M}_x(y,t) \\ \tilde{Q}_x(y,t) \\ \tilde{Q}_z(y,t) \end{Bmatrix} = \begin{bmatrix} \mathcal{A}_1^{Mx}\sin\beta(y) & \mathcal{A}_3^{Mz}\cos\beta(y) \\ \mathcal{A}_1^{Mx}\cos\beta(y) & -\mathcal{A}_3^{Mz}\sin\beta(y) \\ \mathcal{A}_1^{Qx}\cos\beta(y) & \mathcal{A}_3^{Qz}\sin\beta(y) \\ -\mathcal{A}_1^{Qx}\sin\beta(y) & \mathcal{A}_3^{Qz}\cos\beta(y) \end{bmatrix} \begin{Bmatrix} V_1(t) \\ V_3(t) \end{Bmatrix} P(y). \tag{25}$$

5.3. Linear governing equations

In view of physically evidence fact that the blade is much stiffer in the longitudinal direction than in the flapping and lagging ones, the effect of the axial inertia is much smaller than the others. Thus discarding axial inertial term $b_1\ddot{v}_0$ and Coriolis effect term $2b_1\Omega\dot{v}_0$ (which is negligibly small for this particular blade orientation [35]), the direct integration of Eq. (16b) in conjunction with boundary condition at the free end, stipulating zero external forces ($p_y = 0$,

$\tilde{T}_y = 0$) yields

$$T_y(y,t) \approx -\int_y^L \left\{-b_1\Omega^2(R_0 + y + v_0)\right\} \mathrm{d}\, y = b_1\Omega^2 R(y) = \hat{T}_y(y,t), \tag{26}$$

where over-hat $(\hat{\cdot})$ denotes the force induced by dynamical (centrifugal) stiffening effect and

$$R(y) = R_0(L-y) + \frac{1}{2}(L^2 - y^2). \tag{27}$$

Note that, for high angular speed Ω, this dynamic stiffening effect will be significant and should be included in the linear system. In addition, as concerns Eq. (16d) governing the twist-extension motion, $\hat{\Gamma}_t$ which plays the role of a torsional stiffness induced by the centrifugal force field should also be considered [8],

$$\hat{\Gamma}_t = (b_4 + b_5)\Omega^2 R(y). \tag{28}$$

Taking Eqs. (20), (21), (24) and (25) into the governing equations and the associated boundary conditions (Eqs. (16)-(18)) in conjunction with Eqs. (26) and (28), the system can be linearized in the CUS lay-up configuration. Actually the linear system can be split into two subsystems, one governs the lateral bending-vertical bending coupling motion (flap-lag) and the other governs the twist-extension coupling motion.

BB-subsystem (Lateral ***B****ending-Vertical* ***B****ending coupling).*

$$\begin{aligned}
\delta u_0 \,:\, & [a_{24}\theta_z' + a_{34}\theta_x' + a_{44}(u_0' + \theta_z) + a_{45}(w_0' + \theta_x)]' + p_x + \underline{b_1\Omega^2[R(y)u_0']'} \\
& - b_1[\ddot{u}_0 - \underline{2\Omega\dot{v}_0} - \underline{\Omega^2 u_0}] + \delta_p P'(y)\left[\mathcal{A}_1^{Qx} V_1 \cos\beta + \mathcal{A}_3^{Qz} V_3 \sin\beta\right] \\
& + \beta' P(y)\left[-\mathcal{A}_1^{Qx} V_1 \sin\beta + \mathcal{A}_3^{Qz} V_3 \cos\beta\right] = 0,
\end{aligned} \tag{29a}$$

$$\begin{aligned}
\delta w_0 \,:\, & [a_{25}\theta_z' + a_{35}\theta_x' + a_{45}(u_0' + \theta_z) + a_{55}(w_0' + \theta_x)]' + \underline{b_1\Omega^2[R(y)w_0']'} \\
& - b_1\ddot{w}_0 + p_z + \delta_p P'(y)\left[\mathcal{A}_3^{Qz} V_3 \cos\beta - \mathcal{A}_1^{Qx} V_1 \sin\beta\right] \\
& - \beta' P(y)\left[\mathcal{A}_3^{Qz} V_3 \sin\beta + \mathcal{A}_1^{Qx} V_1 \cos\beta\right] = 0,
\end{aligned} \tag{29b}$$

$$
\begin{aligned}
\delta\theta_x\ :\ & \big[a_{23}\theta_z' + a_{33}\theta_x' + a_{34}(u_0' + \theta_z) + a_{35}(w_0' + \theta_x)\big]' - \big[a_{25}\theta_z' + a_{35}\theta_x' \\
& + a_{45}(u_0' + \theta_z) + a_{55}(w_0' + \theta_x)\big] + m_x - b_4\ddot{\theta}_x - b_6\ddot{\theta}_z - 2\Omega b_4\dot{\phi} \\
& + \underline{\underline{\Omega^2(b_4\theta_x + b_6\theta_z)}} + \delta_p P'(y)\left[\mathcal{A}_1^{Mx} V_1 \cos\beta - \mathcal{A}_3^{Mz} V_3 \sin\beta\right] \\
& + P(y)\big[(-\mathcal{A}_1^{Mx}\beta' + \mathcal{A}_1^{Qx})V_1 \sin\beta - (\mathcal{A}_3^{Mz}\beta' + \mathcal{A}_3^{Qz})V_3\cos\beta\big] = 0,
\end{aligned}
\tag{29c}
$$

$$
\begin{aligned}
\delta\theta_z\ :\ & \big[a_{22}\theta_z' + a_{23}\theta_x' + a_{24}(u_0' + \theta_z) + a_{25}(w_0' + \theta_x)\big]' - \big[a_{24}\theta_z' + a_{34}\theta_x' \\
& + a_{44}(u_0' + \theta_z) + a_{45}(w_0' + \theta_x)\big] + m_z - b_5\ddot{\theta}_z - b_6\ddot{\theta}_x - 2\Omega b_6\dot{\phi} \\
& + \underline{\underline{\Omega^2(b_5\theta_z + b_6\theta_x)}} + \delta_p P'(y)\left[\mathcal{A}_3^{Mz} V_3 \cos\beta + \mathcal{A}_1^{Mx} V_1 \sin\beta\right] \\
& - P(y)\big[(\mathcal{A}_3^{Mz}\beta' + \mathcal{A}_3^{Qz})V_3 \sin\beta - (\mathcal{A}_1^{Mx}\beta' - \mathcal{A}_1^{Qx})V_1\cos\beta\big] = 0,
\end{aligned}
\tag{29d}
$$

the boundary conditions are

at $y = 0$:

$$
u_0 = w_0 = \theta_x = \theta_z = 0, \tag{30}
$$

and at $y = L$:

$$
\begin{aligned}
\delta u_0\ :\ & a_{24}(L)\theta_z' + a_{34}(L)\theta_x' + a_{44}(L)(u_0' + \theta_z) + a_{45}(L)(w_0' + \theta_x) \\
& + \delta_s\left[\mathcal{A}_1^{Qx} V_1 \cos\beta(L) + \mathcal{A}_3^{Qz} V_3 \sin\beta(L)\right] = \bar{Q}_x,
\end{aligned}
\tag{31a}
$$

$$
\begin{aligned}
\delta w_0\ :\ & a_{25}(L)\theta_z' + a_{35}(L)\theta_x' + a_{45}(L)(u_0' + \theta_z) + a_{55}(L)(w_0' + \theta_x) \\
& + \delta_s\left[\mathcal{A}_3^{Qz} V_3 \cos\beta(L) - \mathcal{A}_1^{Qx} V_1 \sin\beta(L)\right] = \bar{Q}_z,
\end{aligned}
\tag{31b}
$$

$$
\begin{aligned}
\delta\theta_x\ :\ & a_{23}(L)\theta_z' + a_{33}(L)\theta_x' + a_{34}(L)(u_0' + \theta_z) + a_{35}(L)(w_0' + \theta_x) \\
& + \delta_s\left[\mathcal{A}_1^{Mx} V_1 \cos\beta(L) - \mathcal{A}_3^{Mz} V_3 \sin\beta(L)\right] = \bar{M}_x,
\end{aligned}
\tag{31c}
$$

$$
\begin{aligned}
\delta\theta_z\ :\ & a_{22}(L)\theta_z' + a_{23}(L)\theta_x' + a_{24}(L)(u_0' + \theta_z) + a_{25}(L)(w_0' + \theta_x) \\
& + \delta_s\left[\mathcal{A}_3^{Mz} V_3 \cos\beta(L) + \mathcal{A}_1^{Mx} V_1 \sin\beta(L)\right] = \bar{M}_z.
\end{aligned}
\tag{31d}
$$

*TE-subsystem (**T**wist-**E**xtension coupling).*

$$
\begin{aligned}
\delta v_0 \ &: a_{11} v_0'' + a_{17}\phi'' + p_y + \delta_p P'(y)[\mathcal{A}_2^{Ty} V_2 + \mathcal{A}_4^{Ty} V_4] \\
&- b_1[\ddot{v}_0 + 2\Omega\dot{u}_0 - \underline{\Omega^2(R_0 + y + v_0)}] = 0,
\end{aligned}
\tag{32a}
$$

$$
\begin{aligned}
\delta\phi \ &: a_{17} v_0'' + a_{77}\phi'' - a_{66}\phi^{(iv)} + m_y + b_w' + \delta_p P'(y)[\mathcal{A}_2^{My} V_2 + \mathcal{A}_4^{My} V_4] \\
&- (b_4 + b_5)\ddot{\phi} + b_{10}\ddot{\phi}'' + 2\Omega(b_4\dot{\theta}_x + b_6\dot{\theta}_z) + \Omega^2\left[b_6 + (b_4 - b_5 - b_6)\phi\right] \\
&+ \underline{\Omega^2[(b4 + b5)R(y)\phi']'} - b_{10}\Omega^2\phi'' = 0,
\end{aligned}
\tag{32b}
$$

the boundary conditions are

at $y = 0$:

$$
v_0 = \phi = \phi' = 0,
\tag{33}
$$

and at $y = L$:

$$
\delta v_0 \ : a_{11} v_0' + a_{17}\phi' + \delta_s[\mathcal{A}_2^{Ty} V_2 + \ \mathcal{A}_4^{Ty} V_4] = \bar{T}_y,
\tag{34a}
$$

$$
\begin{aligned}
\delta\phi \ &: a_{17} v_0' + a_{77}\phi' - a_{66}'''\phi + b_{10}(\ddot{\phi}' - \Omega^2\phi') \\
&+ \delta_s[\mathcal{A}_2^{My} V_2 + \delta_s\mathcal{A}_4^{My} V_4] = \bar{M}_y,
\end{aligned}
\tag{34b}
$$

$$
\delta\phi' \ : \ a_{66}\phi'' = \bar{B}_w,
\tag{34c}
$$

In these equations, for the cases (a) the actuator is spread over the entire beam span (b) the actuator is a single patch, the traces have to be taken as (a) $\delta_p = 0$ and $\delta_s = 1$ (b) $\delta_p = 1$ and $\delta_s = 0$, respectively. Note that, the two subsystems are independent when Coriolis effects are discarded.

6. Solution methodology

6.1. The Extend Galerkin's Method

The Extend Galerkin's Method (EGM) [36, 37, 33] is applied to discretize the system for numerical study. The underlying idea of EGM is to select weighting (or shape) functions that exactly satisfy only the geometric boundary conditions ($y = 0$). The terms arising as a result of the non-fulfillment of natural boundary conditions ($y = L$) remain as residual terms in the energy functional itself, which are then minimized in the Galerkin sense [38], thus yielding excellent accuracy and rapid convergence [37]. Let

$$\begin{gathered} u_0(y,t) = \boldsymbol{\Psi}_u^T(y)\mathbf{q}_u(t), \quad v_0(y,t) = \boldsymbol{\Psi}_v^T(y)\mathbf{q}_v(t), \quad w_0(y,t) = \boldsymbol{\Psi}_w^T(y)\mathbf{q}_w(t), \\ \phi_((y,t) = \boldsymbol{\Psi}_\phi^T(y)\mathbf{q}_\phi(t), \quad \theta_x(y,t) = \boldsymbol{\Psi}_x^T(y)\mathbf{q}_x(t), \quad \theta z(y,t) = \boldsymbol{\Psi}_z^T(y)\mathbf{q}_z(t), \end{gathered} \tag{35}$$

where the shape functions $\boldsymbol{\Psi}_u^T(y)$, $\boldsymbol{\Psi}_v^T(y)$, $\boldsymbol{\Psi}_w^T(y)$, $\boldsymbol{\Psi}_\phi^T(y)$, $\boldsymbol{\Psi}_x^T(y)$ and $\boldsymbol{\Psi}_z^T(y)$ are required to fulfill the geometric boundary conditions. Thus the discretized forms of the BB- and TE-subsystems follow as

$$\mathbf{M}_{B/T}\ddot{\mathbf{q}}_{B/T} + [\mathbf{K}_{B/T} + \Omega^2\hat{\mathbf{K}}_{B/T}]\mathbf{q}_{B/T} + \mathcal{A}_{B/T}\mathbf{V}_{B/T} = \mathbf{Q}_{B/T}, \tag{36}$$

where

$$\mathbf{q}_B = \begin{Bmatrix} \mathbf{q}_u^T & \mathbf{q}_w^T & \mathbf{q}_x^T & \mathbf{q}_z^T \end{Bmatrix}^T, \quad \mathbf{q}_T = \begin{Bmatrix} \mathbf{q}_v^T & \mathbf{q}_\phi^T \end{Bmatrix}^T, \tag{37}$$

$$\mathbf{V}_B = \begin{Bmatrix} V_1 & V_3 \end{Bmatrix}^T, \quad \mathbf{V}_T = \begin{Bmatrix} V_2 & V_4 \end{Bmatrix}^T. \tag{38}$$

The subscript B and T denote the matrix/vector of BB- and TE-subsystems, respectively. The expressions for mass matrix $\mathbf{M}_{B/T}$, stiffness matrix $\mathbf{K}_{B/T}$, additional stiffness matrix $\hat{\mathbf{K}}_{B/T}$, actuating matrix $\mathcal{A}_{B/T}$ and external excitation vector $\mathbf{Q}_{B/T}$ are given in Appendix D.

6.2. *Negative velocity feedback control*

We assume the sensor can offer the velocity information at the beam span $y = Y_s$, then the actuating voltage vector $\mathbf{V}_{B/T}$ for the negative velocity feedback control algorithm [39, 31] can be rewritten as

$$\begin{aligned} \mathbf{V}_B = \begin{Bmatrix} V_1 \\ V_3 \end{Bmatrix} &= \begin{Bmatrix} -k_1[-\dot{\theta}_x^p(Y_s,t)] \\ -k_3[\dot{\theta}_z^p(Y_s,t)] \end{Bmatrix} \\ &= \begin{Bmatrix} k_1[\dot{\theta}_x(Y_s,t)\cos\beta + \dot{\theta}_z(Y_s,t)\sin\beta] \\ -k_3[-\dot{\theta}_x(Y_s,t)\sin\beta + \dot{\theta}_z(Y_s,t)\cos\beta] \end{Bmatrix} = \mathbf{P}_B(Y_s)\dot{\mathbf{q}}_B(t), \end{aligned} \tag{39}$$

$$\mathbf{V}_T = \begin{Bmatrix} V_2 \\ V_4 \end{Bmatrix} = \begin{Bmatrix} -k_2\dot{\phi}^p(Y_s,t) \\ -k_4\dot{\phi}^p(Y_s,t) \end{Bmatrix} = \begin{Bmatrix} -k_2\dot{\phi}(Y_s,t) \\ -k_4\dot{\phi}(Y_s,t) \end{Bmatrix} = \mathbf{P}_T(Y_s)\dot{\mathbf{q}}_T(t), \tag{40}$$

where, k_i $(i = 1, 2, 3, 4)$ are defined as feedback control gains. The expressions of control matrices $\mathbf{P}_{B/T}$ are given in Appendix D. As a result, the closed-loop dicretized system Eq. (36) becomes

$$\mathbf{M}_{B/T}\ddot{\mathbf{q}}_{B/T}(t) + \mathcal{A}_{B/T}\mathbf{P}_{B/T}\dot{\mathbf{q}}_{B/T}(t) + [\mathbf{K}_{B/T} + \Omega^2\hat{\mathbf{K}}_{B/T}]\mathbf{q}_{B/T}(t) = \mathbf{Q}_{B/T}(t). \tag{41}$$

7. Model validations

The model validation is implemented on two aspects, viz., frequency and actuating performance. At first, Table 1 compares the frequency predictions of an unpretwisted rotating beam with the FEM results in Ref. [40] and the experimental data in Ref. [7], showing good agreements. The geometry and material properties of the box beam used in this validation are shown in Table 2.

Table 3 further compares the frequency predictions of a pretwisted and unrotating beam. The characteristics of the beam are given as [31, p. 275]

$$a_{22}^p = 487.9\ \mathrm{N\cdot m^2}, \quad a_{33}^p = 2.26\ \mathrm{N\cdot m^2}, \quad a_{44}^p = a_{55}^p = 3.076\times10^6\ \mathrm{N\cdot m^2}$$
$$a_{25}^p = a_{34}^p = 0, \quad b_1^p = 0.3447\ \mathrm{kg/m}, \quad b_4^p = 8.57\times10^{-8}\ \mathrm{kg\cdot m},$$
$$b_5^p = 0.19\times10^{-4}\ \mathrm{kg\cdot m}, \quad b_6^p = 0, \quad L = 0.1524\ \mathrm{m}.$$

The present displayed predictions are in good agreement with the results of Ref. [10].

Next, a 1/16th scale blade with NACA 0012 airfoil cross-section of Fig. 5 is used for actuating performance validation. Material properties of E-glass and AFC layers are shown in Table 4. Fig. 6 plots the tip twist angle varying with applied voltage, showing a good agreement with Ref. [41].

Table 1: Frequencies at $\Omega = 1002$ rpm for CUS lay-up configuration (Hz) [a].

	$[75]_6$			$[90/60]_3$		
Mode	Exp. [7]	FEM [40]	Present	Exp. [7]	FEM [40]	Present
Flap 1	36.49	34.63	36.65	39.54	38.71	39.26
Lag 1	53.73	47.31	55.79	56.42	54.38	56.44
Flap 2	202.2	188.0	202.45	222.3	215.8	220.3

[a] $\gamma_0 = \beta_0 = 0$, $\Omega = 1002$ rpm, $R_0 = 0$

Table 2: Details of thin-walled composite box beam for validation [7]

E_{11}	1.42×10^{11} N/m^2	Density (ρ)	1.442×10^3 Kg/m^3
$E_{22} = E_{33}$	9.8×10^9 N/m^2	Width ($2b^a$)	2.268×10^{-2} m
$G_{12} = G_{13}$	6.0×10^9 N/m^2	Depth ($2d^a$)	1.212×10^{-2} m
G_{23}	4.83×10^9 N/m^2	Number of layers (N_h)	6
$\mu_{12} = \mu_{13}$	0.42	Layer thickness	1.270×10^{-4} m
μ_{23}	0.50	Length (L)	0.8446 m

[a] Inner dimensions of the cross section.

Table 3: Comparison of coupled flapping-lagging frequencies of a pretwisted beam [a] (Hz).

Mode	1BB	2BB	3BB	4BB
Ref. [10]	62.0	305.1	949.0	1206.1
Present	62.1	305.3	951.3	1209.2

[a] $\gamma_0 = 0$, $\beta_0 = 45^o$, $\Omega = 0$, $R_0 = 0$

8. Numerical study and discussion

Although the governing equations are valid for a thin-walled beam with an arbitrary closed-cross section, for the sake of illustration, the beam with a typical rectangular cross-section of Fig. 2 is considered here. Material properties and geometric specifications of the host structure are shown in Table 5. The piezo-actuator is manufactured by signal crystal MFC, whose material properties are given in Table 4. We assume the piezo-actuators are spread over the entire beam span and bonded outside the host structure. The lay-up configurations

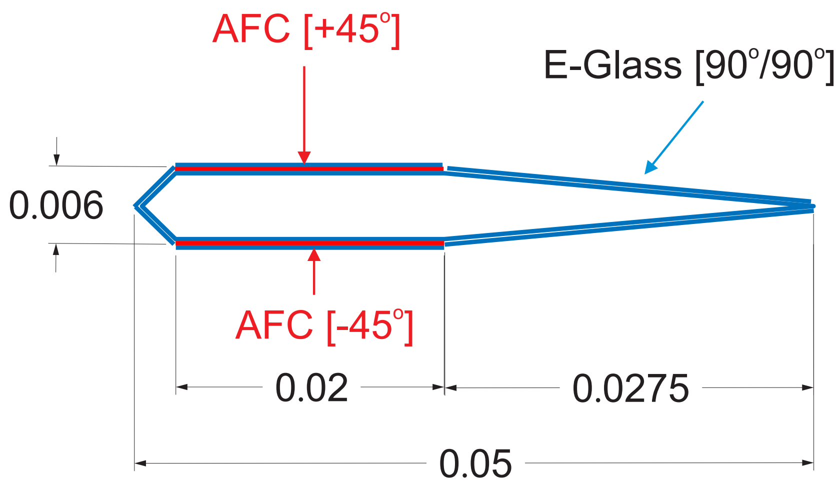

Figure 5: NACA0012 airfoil cross-section (unit: m)

Table 4: Material properties of E-glass, AFC, and single crystal MFC (S-MFC)

Material property	E-Glass [41]	AFC [41]	S-MFC [42]
E_1 (Gpa)	14.8	30.54	6.23
E_2 (Gpa)	13.6	16.11	11.08
G_{12} (Gpa)	1.9	5.5	2.01
μ_{12}	0.19	0.36	0.229
d_{11} ($\times 10^{-12}$ m/V)	N/A	381	1896.5
d_{12} ($\times 10^{-12}$ m/V)	N/A	-160	-838.2
ρ (Kg m^{-3})	1700	4810	5338.3
Thickness ($\times 10^{-4}$ m)	2.032	1.689	17
Electrode spacing ($\times 10^{-3}$ m)	N/A	1.143	1.7

for the host structure and the piezo-actuator are listed in Table 6. The sensor is located at the beam tip, i.e., $Y_s = L$.

8.1. Study of piezo-actuator coefficients

The piezo-actuator coefficients $\mathcal{A}_i^X$ appearing in Eqs. (24) and (25) are plotted as a function of piezo-actuator ply-angle θ_p in Figs. 7 and 8. Note that, the

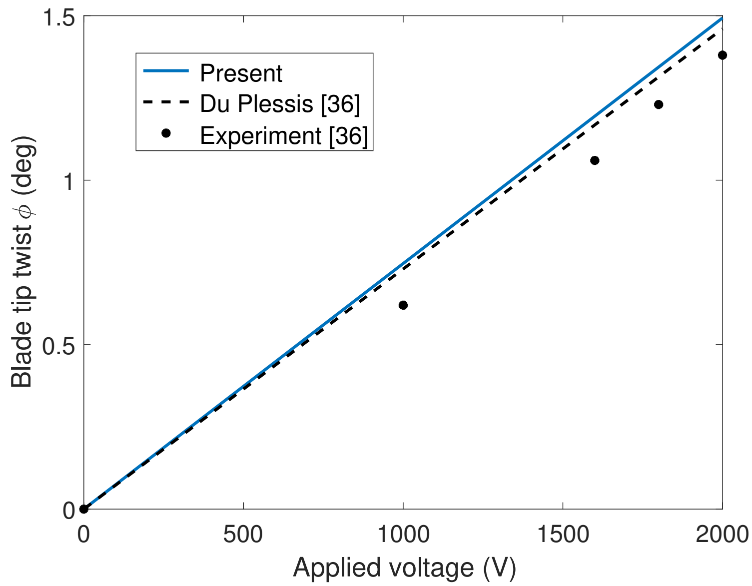

Figure 6: Tip deflection for NACA 0012 airfoil

Table 5: Material properties (Graphite-Epoxy) and geometric specifications of the thin-walled box beam

Material	**Value**	**Geometric**	**Value**
E_{11}	206.8×10^9 N/m^2	Width ($2b^a$)	0.254 m
$E_{22} = E_{33}$	5.17×10^9 N/m^2	Depth ($2d^a$)	0.0681 m
$G_{12} = G_{13}$	2.55×10^9 N/m^2	Wall thickness (h)	0.0102 m
G_{23}	3.10×10^9 N/m^2	Number of layers (N_h)	6
$\mu_{12} = \mu_{13} = \mu_{23}$	0.25	Layer thickness	0.0017 m
ρ	1.528×10^3 Kg/m^3	Length (L)	2.032 m

[a] The length is measured on the mid-line contour.

piezo-actuator coefficients appearing in BB- and TE-subsystems are indicated by solid and dashed lines, respectively. Two distinct trends can be concluded in

Table 6: CUS lay-up configurations (deg) [a]

		Flanges		Webs	
Layer	Material	Top	Bottom	Left	Right
CUS (7)	Piezo-actuator	$[\theta_p]$	$[\theta_p]$	$[\theta_p]$	$[\theta_p]$
CUS (1-6)	Host structure	$[\theta_h]_6$	$[\theta_h]_6$	$[\theta_h]_6$	$[\theta_h]_6$

[a] θ_p and θ_h denote the ply-angles in piezo-actuator and host structure.

the results of Figs. 7 and 8. One including bending coefficients ($\mathcal{A}_1^{Mx}$, $\mathcal{A}_3^{Mz}$) [1] and extension coefficients ($\mathcal{A}_2^{Ty}$, $\mathcal{A}_4^{Ty}$) shows a symmetric dependence centered around $\theta_p = 90^o$. The other characterizing transverse shear coefficients ($\mathcal{A}_1^{Qx}$, $\mathcal{A}_3^{Qz}$) and twist coefficients ($\mathcal{A}_2^{My}$ and $\mathcal{A}_4^{My}$), instead, presents an anti-symmetric trend. Moreover, their values equal to zero when $\theta_p = 0^o,\ 90^o, 180^o$, and their maximum absolute values reached for $\theta_p \approx 42,\ 138^o$.

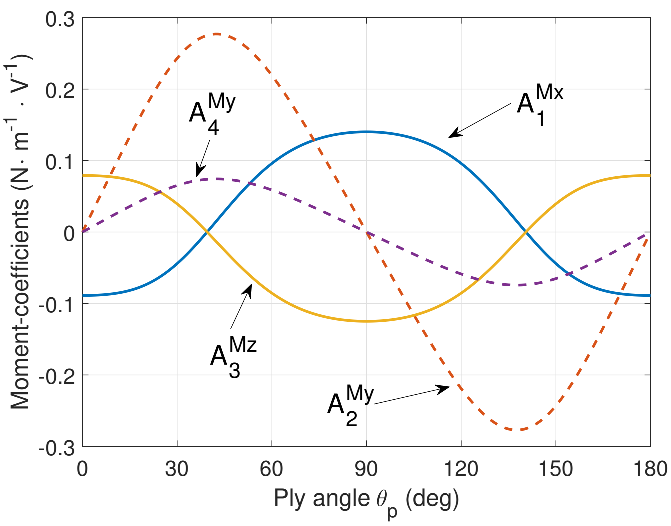

Figure 7: Actuating moment coefficients as a function of piezo-actuator ply-angle θ_p in CUS lay-up configuration.

[1] The reason for $\mathcal{A}_1^{Mx}$ and $\mathcal{A}_3^{Mz}$ exhibiting the opposite trends is the reverse definition of θ_x in Fig. 2.

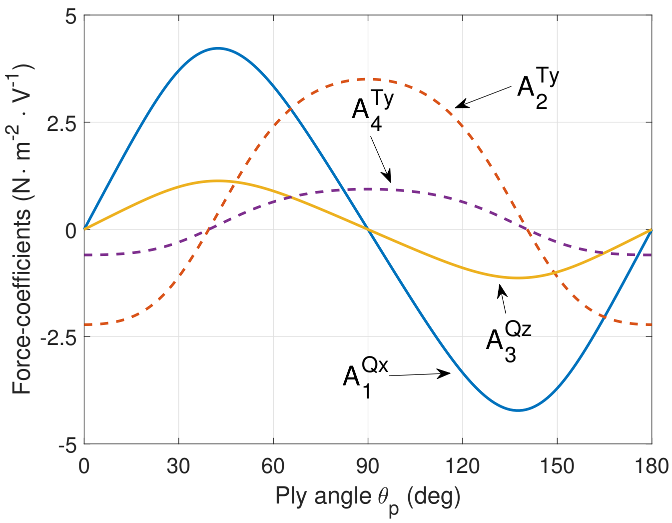

Figure 8: Actuating force coefficients as a function of piezo-actuator ply-angle θ_p in CUS lay-up configuration.

8.2. Study of anisotropic characteristic of piezo-composite

8.2.1. BB-subsystem

Considering that the lateral bending-vertical bending elastic coupling has a significant effect on flapping and lagging motions, the weak and strong elastic coupling cases should be investigated separately. For an unpretwisted beam, the elastic coupling is just related to stiffness coefficients $a_{25} = a_{25}^p$ and $a_{34} = a_{34}^p$ [33]. Fig. 9 depicts all non-zero stiffness coefficients a_{ij}^p in BB-subsystem as a function of host ply-angle θ_h. It can be seen that a_{25}^p and a_{34}^p are negligible during $0^o < \theta_h < 30^o$ or $150^o < \theta_h < 180^o$. Thus, $\theta_h = 15^o$ and $\theta_h = 75^o$ are selected to study the weak and strong elastic coupling cases, respectively.

Figures 10 and 11 plot damping ratios of the first four modes as a function of piezo-actuator ply-angle θ_p for the weak and strong elastic coupling cases, respectively. The damping ratios in Figs. 10 and 11 follow the trend of coefficients ($\mathcal{A}_1^{Mx}$, $\mathcal{A}_3^{Mz}$) in Fig. 7 and ($\mathcal{A}_1^{Qx}$, $\mathcal{A}_3^{Qz}$) in Fig. 8, respectively. This implies that bending moment actuation and transverse shear force actuation

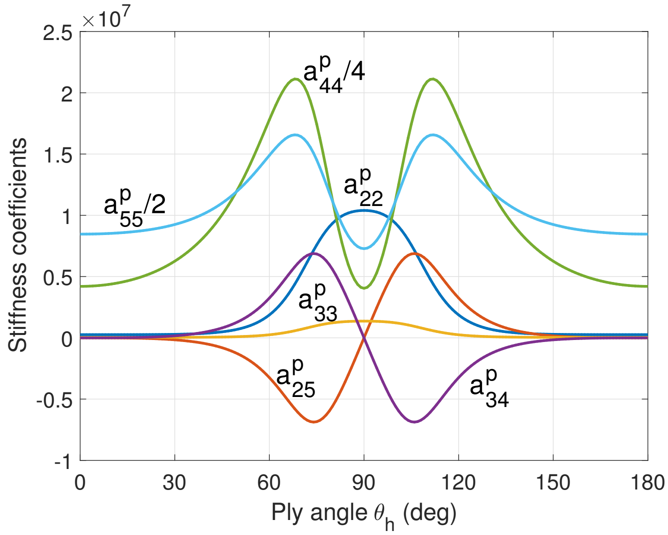

Figure 9: Stiffness coefficients a_{ij}^{p} as a function of host structure ply-angle θ_h in BB-subsystem; units: a_{22}^{p} $(\mathrm{N}\cdot\mathrm{m}^2)$, a_{25}^{p} $(\mathrm{N}\cdot\mathrm{m})$, a_{33}^{p} $(\mathrm{N}\cdot\mathrm{m}^2)$, a_{34}^{p} $(\mathrm{N}\cdot\mathrm{m})$, a_{44}^{p} (N) and a_{55}^{p} (N).

play the dominate role in weak and strong elastic coupling cases, respectively. As a result, the optimum piezo-actuator ply-angle for $\theta_h = 15^o$ and $\theta_h = 75^o$ cases are $\theta_p = 90^o$ and $\theta_p = 130^o$, respectively.

8.2.2. TE-subsystem

Figure 12 depicts damping ratios of the first three twist modes as a function of θ_p for selected two host structure cases, i.e., $\theta_h = 15^o$ and $\theta_h = 75^o$. It can been seen that $\theta_p \approx 135^o$ yields the best twist control authority.

8.3. Study of host structure tailoring

8.3.1. BB-subsystem

Figure 13 plots frequencies of the first four modes of BB-subsystem as a function of host ply-angle θ_h. According to the weak and strong elastic coupling cases, it is reasonable to split the domain of θ_h into "Decoupling" and "Couping" two parts, see Fig. 13. Note that, according to their mode shapes, the first four modes of BB-subsystem can also be denoted as Flap1, Lag1, Flap2 and Lag2 for

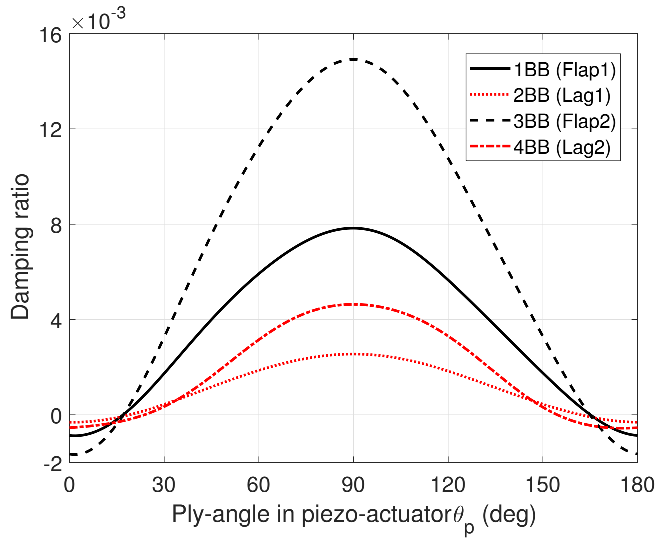

Figure 10: Damping ratios of BB-subsystem ($\theta_h = 15^o$) as a function of piezo-actuator ply-angle θ_p; $k_1 = k_3 = 100$, $\Omega = 0$, $\gamma_0 = \beta_0 = 0$.

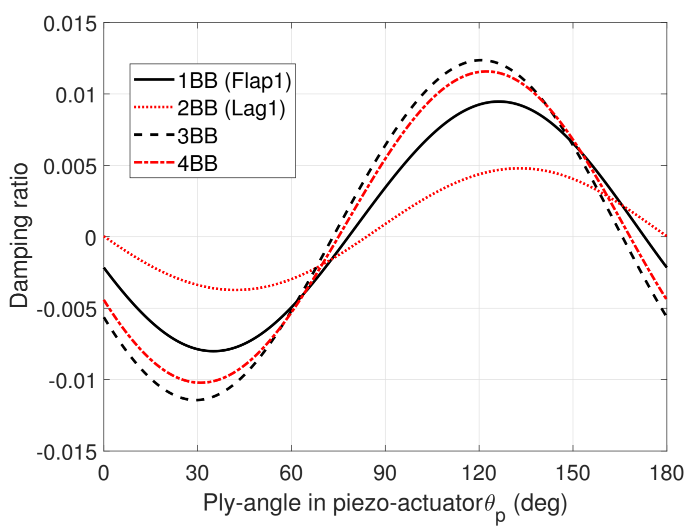

Figure 11: Damping ratios of BB-subsystem ($\theta_h = 75^o$) as a function of piezo-actuator ply-angle θ_p; $k_1 = k_3 = 100$, $\Omega = 0$, $\gamma_0 = \beta_0 = 0$.

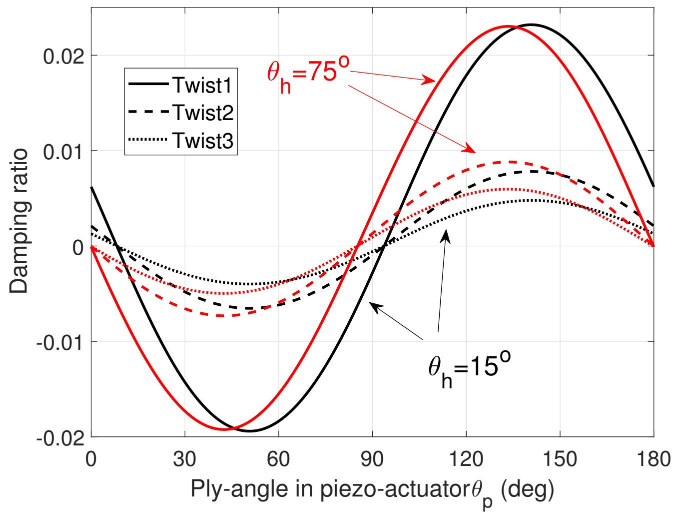

Figure 12: Damping ratios of TE-subsystem as a function of piezo-actuator ply-angle θ_p; $k_2 = k_4 = 10$, $\Omega = 0$, $\gamma_0 = \beta_0 = 0$.

weak elastic coupling cases. However, there will be no pure flapping or lagging modes for strong elastic coupling cases.

Damping ratios of the first four modes of BB-subsystem are highlighted in Figs. 14 and 15 for selected two piezo-actuator ply-angle cases, viz., $\theta_h = 90^o$ (bending moment actuation dominated) and $\theta_p = 130^o$ (transverse shear force actuation dominated). It can be seen that host ply-angle θ_h has a significant effect on damping ratios. $\theta_p = 90^o$ and $\theta_p = 130^o$ would be the better choice for weak and strong elastic coupling cases, respectively.

8.3.2. TE-subsystem

A typical extension mode cross phenomenon can be seen in Fig. 16, which depicts frequencies of TE-subsystem as a function of θ_h. The results of Fig. 17 show that host ply-angle θ_h has a significant effect on damping ratios of the twist modes. Note that, the damping ratios change suddenly during the mode cross regions in Fig. 17, and this can be seen more clearly in Fig. 18 that depicts the damping ratios for $\theta_p = 90^o$ case. In $\theta_p = 90^o$ case, the direct twist actuations

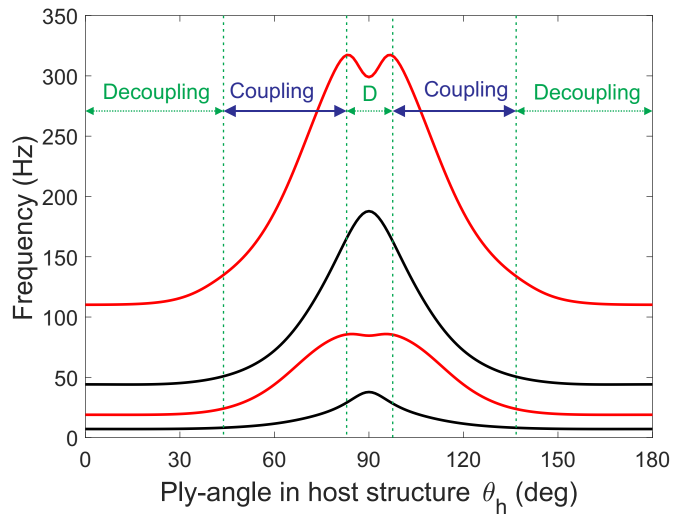

Figure 13: Frequencies of BB-subsystem as a function of host structure ply-angle θ_h; $\Omega = 0$, $\gamma_0 = \beta_0 = 0$.

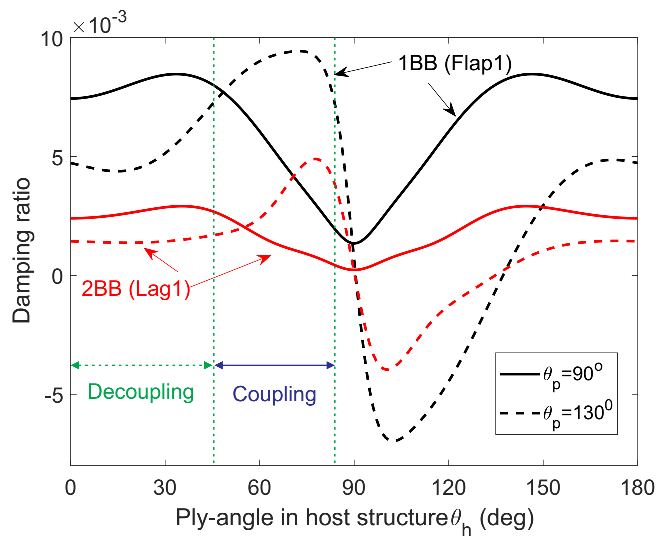

Figure 14: Damping ratios of BB-subsystem as a function of host structure ply-angle θ_h; $k_1 = k_3 = 100$, $\Omega = 0$, $\gamma_0 = \beta_0 = 0$.

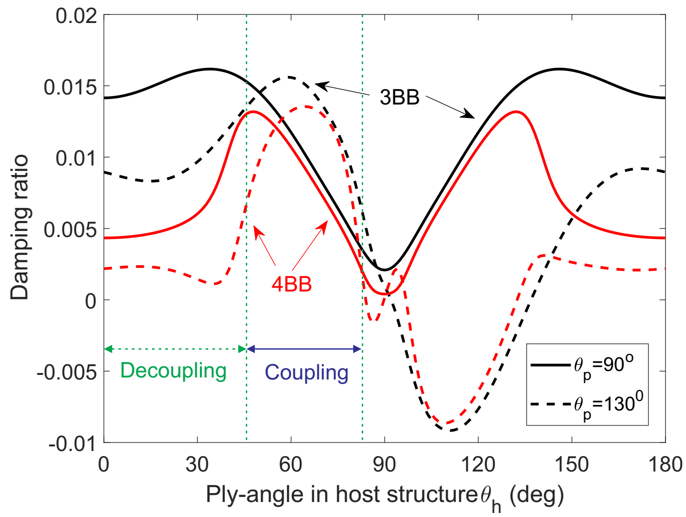

Figure 15: Damping ratios of BB-subsystem as a function of host structure ply-angle θ_h; $k_1 = k_3 = 100$, $\Omega = 0$, $\gamma_0 = \beta_0 = 0$.

($\mathcal{A}_2^{My}$, $\mathcal{A}_4^{My}$) are immaterial. Damping ratios of the twist modes are induced by the extension actuations ($\mathcal{A}_2^{Ty}$, $\mathcal{A}_4^{Ty}$) via the twist-extension elastic coupling.

8.4. Study of rotor speed and presetting angle

8.4.1. BB-subsytem

Figures 19 plots frequencies of the first three modes of BB-subsystem as a function of rotating speed Ω for the weak elastic coupling case. Since centrifugal stiffening effect is more significant in flapping modes than in lagging modes, a frequency crossing of fundamental lagging and flapping modes can be seen in Fig. 19 for the un-presetting beam ($\gamma_0 = 0$). In addition, both in Figs. 19 and 20, it can be found that depending on the flapping and lagging modes, the increase of presetting angle γ_0 yields either an enhance or weaken effect on centrifugal stiffening effect, respectively. The results of Fig. 21 present that with the increase of Ω, damping ratios of the flapping modes decrease more significantly than the lagging mode does.

For the strong elastic coupling case, frequencies and damping ratios of the

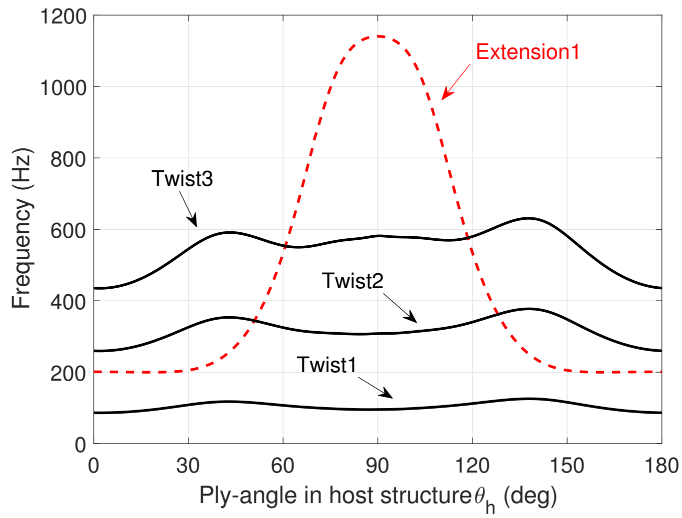

Figure 16: Frequencies of TE-subsystem as a function of host structure ply-angle θ_h; $\Omega = 0$, $\gamma_0 = \beta_0 = 0$

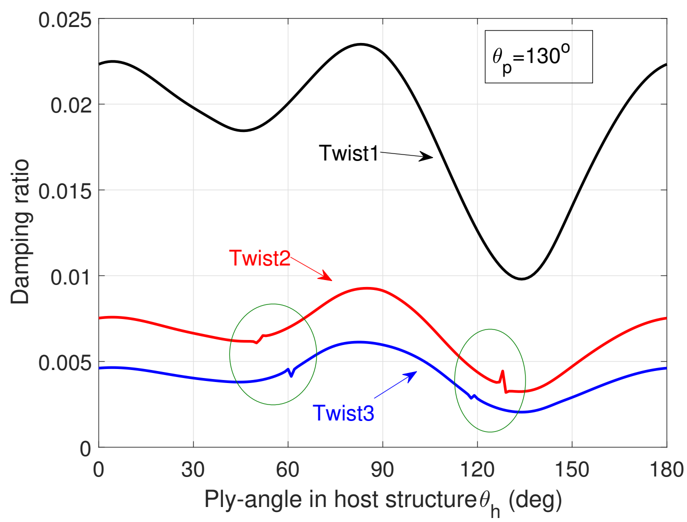

Figure 17: Damping ratios of TE-subsystem as a function of host structure ply-angle θ_h; $k_2 = k_4 = 10$, $\Omega = 0$, $\gamma_0 = \beta_0 = 0$.

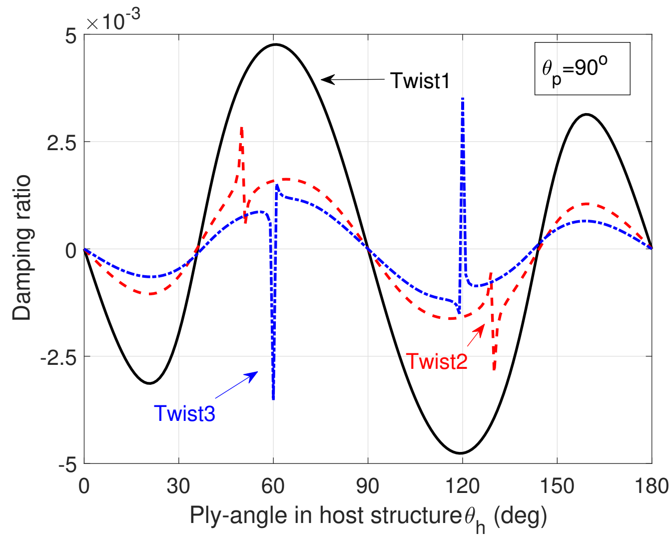

Figure 18: Damping ratios of TE-subsystem as a function of host structure ply-angle θ_h; $k_2 = k_4 = 10$, $\Omega = 0$, $\gamma_0 = \beta_0 = 0$.

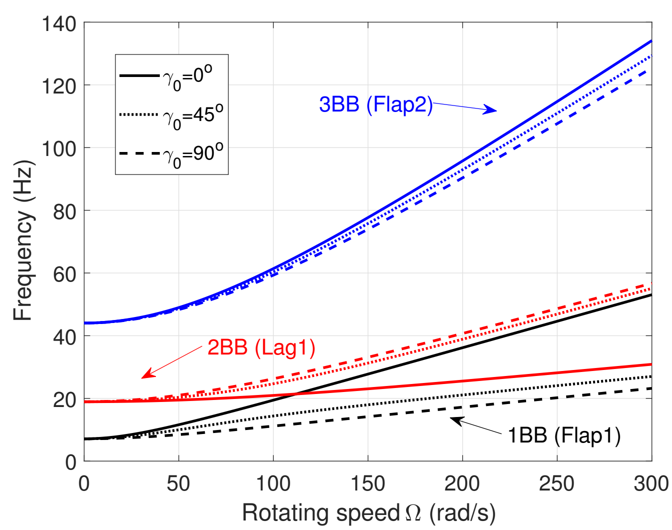

Figure 19: Frequencies of BB-subsystem vs. rotating speed Ω for selected presetting angles γ_0; $\theta_h = 15^o$, $\theta_p = 90^o$, $k_1 = k_3 = 100$, $R_0 = 0.1L$.

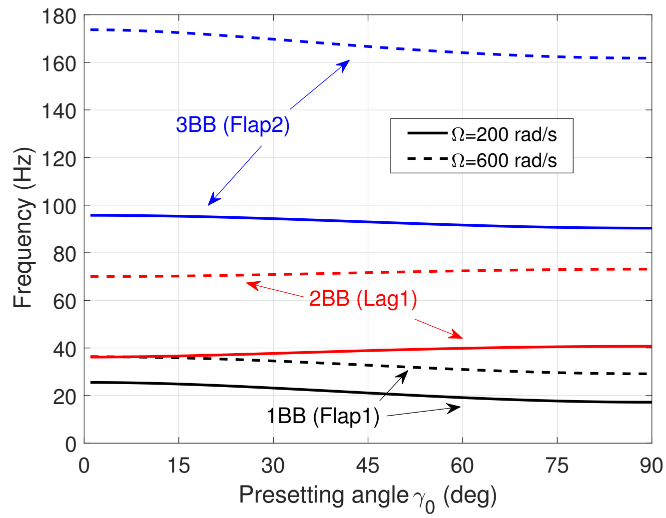

Figure 20: Frequencies of BB-subsystem vs. presetting angle γ_0; $\theta_h = 15^o$, $\theta_p = 90^o$, $k_1 = k_3 = 100$, $R_0 = 0.1L$.

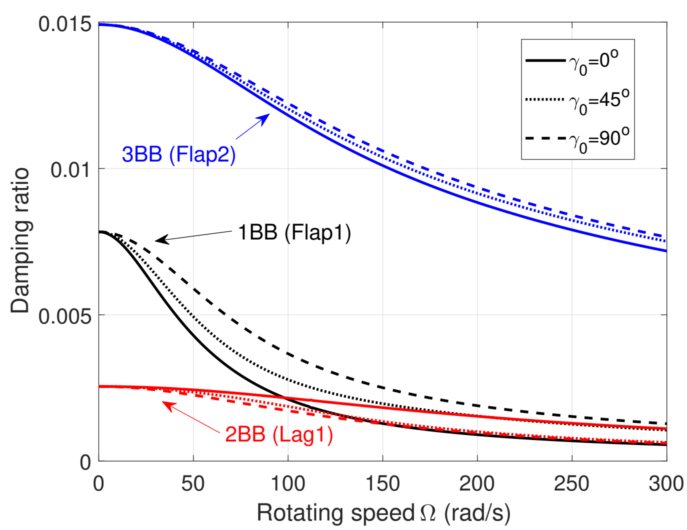

Figure 21: Damping ratios of BB-subsystem vs. rotating speed Ω for selected presetting angles γ_0; $\theta_h = 15^o$, $\theta_p = 90^o$, $k_1 = k_3 = 100$, $R_0 = 0.1L$.

first three modes are shown in Figs. 22 and 23, respectively. Since the elastic coupling will be further enhanced by the centrifugal stiffening effect, in Fig. 22, there is no typical flapping-lagging frequency crossing phenomenon as shown in Fig. 19. During the region near $\Omega \approx 500$ rad/s, the frequencies of 1BB and 2BB modes are very close but not cross for the un-presetting beam ($\gamma_0 = 0$). And their damping ratios present sudden changes during this region, see Fig. 23. The influence of presetting angle γ_0 on the damping ratios for the strong elastic coupling case can be seen more clearly in Fig. 24.

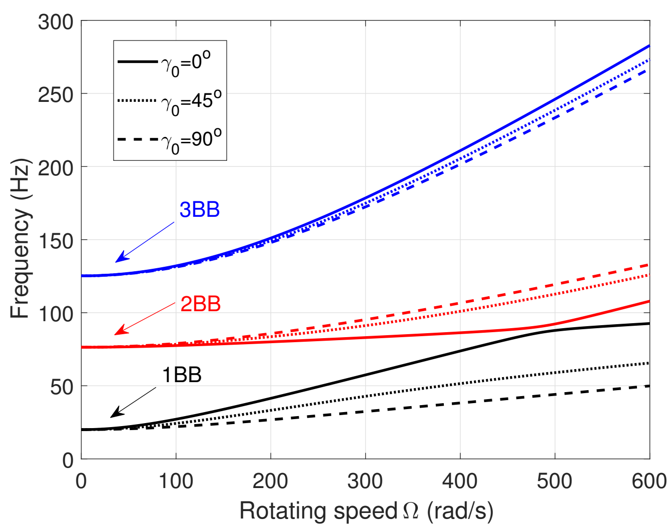

Figure 22: Frequencies of BB-subsystem vs. rotating speed Ω for selected presetting angles γ_0; $\theta_h = 75^o$, $\theta_p = 130^o$, $k_1 = k_3 = 100$, $R_0 = 0.1L$.

8.4.2. TE-subsystem

Figures. 25 and 26 plot frequencies and damping ratios of the first three twist modes as a function of Ω, respectively. The additional torsional stiffness induced by centrifugal force yields an increase of frequency in Fig. 25 and a decrease of damping ratio in Fig. 26. Since the increase of presetting angle γ_0 will yield an increase of the softening tennis-racket term, the fundamental twist frequency exhibits a significant decrease in Fig. 27. However this destiffening

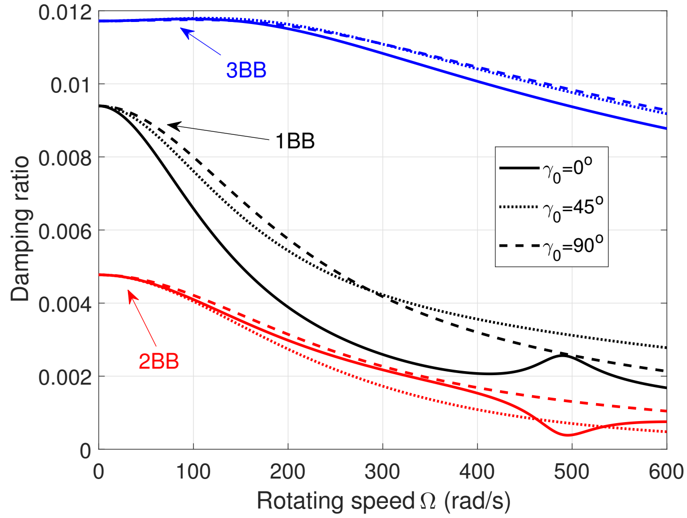

Figure 23: Damping ratios of BB-subsystem vs. rotating speed Ω for selected presetting angles γ_0; $\theta_h = 75^o$, $\theta_p = 130^o$, $k_1 = k_3 = 100$, $R_0 = 0.1L$.

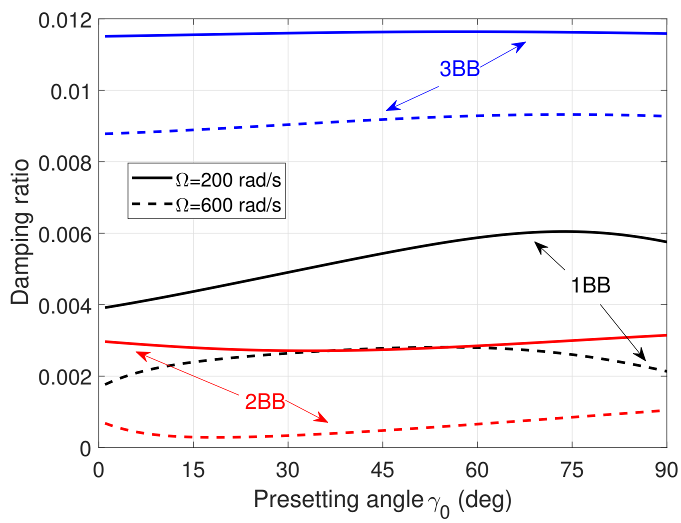

Figure 24: Damping ratios of BB-subsystem vs. presetting angle γ_0; $\theta_h = 75^o$, $\theta_p = 130^o$, $k_1 = k_3 = 100$, $R_0 = 0.1L$.

effect is immaterial for higher twist modes. This conclusion can also be identified in Fig. 28, which highlights the influence of γ_0 on the twist damping ratios. In Fig. 28, with the increase of γ_0, damping ratio of the fundamental twist mode increases until $\gamma_0 \approx 75^o$, then slightly decreases.

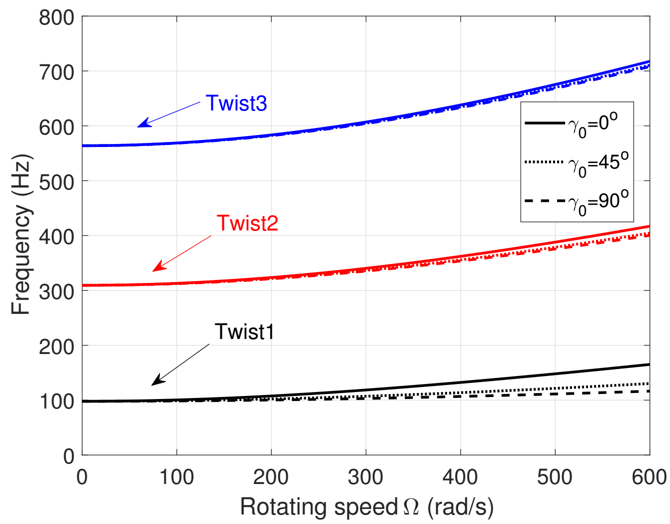

Figure 25: Frequencies of TE-subsystem vs. rotating speed Ω for selected presetting angles γ_0; $\theta_h = 75^o$, $\theta_p = 130^o$, $k_2 = k_4 = 10$, $R_0 = 0.1L$.

8.5. Study of pretwist angle

In order to model helicopter and tilt rotor blades, a special case of Eq. (2) is assumed,

$$\beta(y) = \beta_0 - \beta_0 y/L. \tag{42}$$

This will make the pretwist angle at the beam tip equal to zero, i.e., $\beta(L) = 0$.

8.5.1. BB-subsystem

For fiber-reinforced blades, pretwist angle will make flapping and lagging motions coupled strongly, thus we just consider $\theta_h = 75^o$ this case here. Fig. 29 depicts frequencies of the first three modes of BB-subsystem as a function of pretwist angle β_0. For the unrotating case, the fundamental frequency (1BB) is

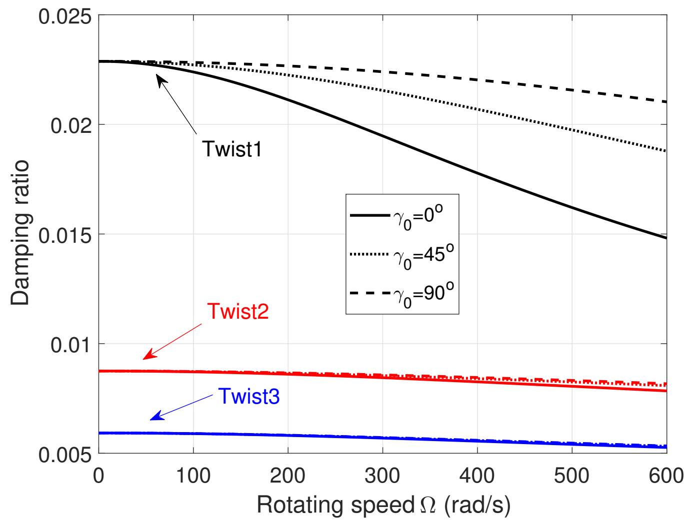

Figure 26: Damping ratios of TE-subsystem vs. rotating speed Ω for selected presetting angles γ_0; $\theta_h = 75^o$, $\theta_p = 130^o$, $k_2 = k_4 = 10$, $R_0 = 0.1L$.

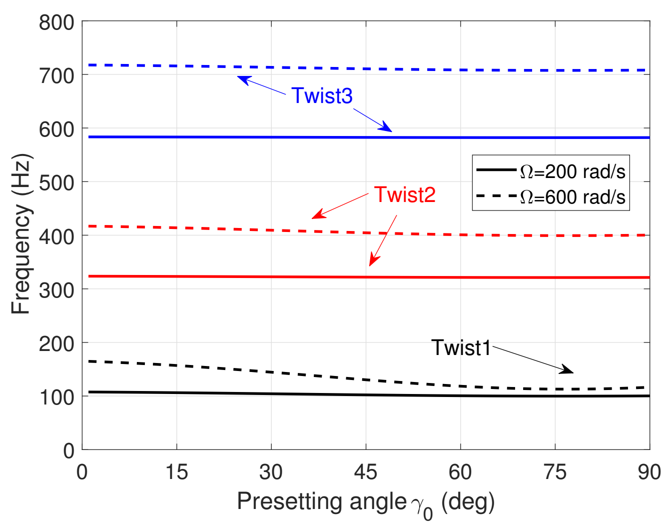

Figure 27: Frequencies of TE-subsystem vs. presetting angle γ_0; $\theta_h = 75^o$, $\theta_p = 130^o$, $k_2 = k_4 = 10$, $R_0 = 0.1L$.

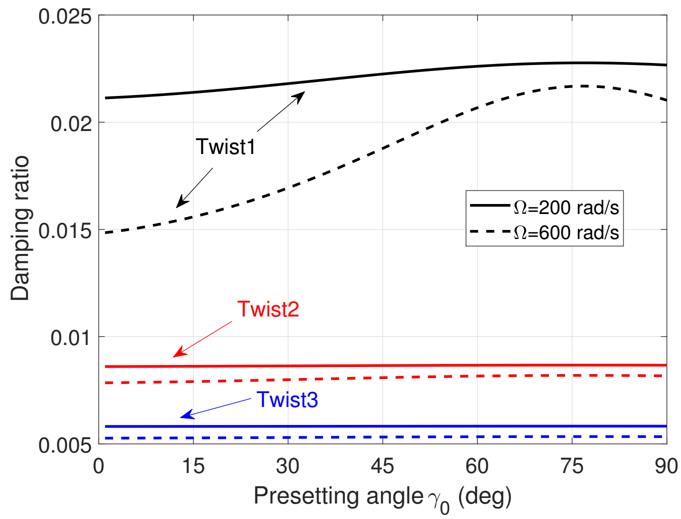

Figure 28: Damping ratios of TE-subsystem vs. presetting angle γ_0; $\theta_h = 75^o$, $\theta_p = 130^o$, $k_2 = k_4 = 10$, $R_0 = 0.1L$.

not sensitive to pretwist angle β_0. However it decreases significantly with the increase of β_0 for the high speed rotating case ($\Omega = 600$ rad/s).

In order to study the relationship between damping ratios and pretwist angle β_0, two piezo-actuator cases, i.e., $\theta_p = 130^o$ (transverse shear force actuation dominated) in Fig. 30 and $\theta_p = 90^o$ (bending moment actuation dominated) in Fig. 31 are considered. According to the previous discussion, we know for the strong elastic coupling case, transverse shear force actuation is more efficient than bending moment actuation when the beam is unpretwisted. However for a pretwisted beam, transverse shear force actuation may lose control for 2BB mode, and even induce a negative damping ratio for the high speed rotating case, see Fig. 30. On the other hand, bending moment actuation can guarantee the balanced positive damping ratios for an arbitrary pretwisted angle β_0, see Fig. 31.

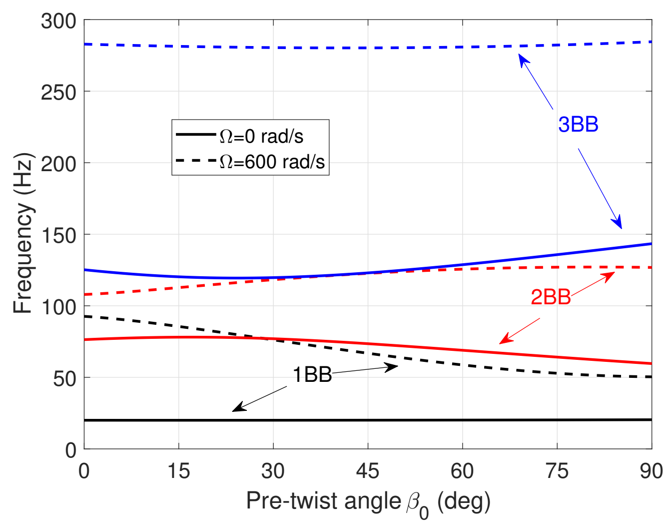

Figure 29: Frequencies of BB-subsystem vs. pretwist angle β_0 for selected rotating speeds Ω; $\theta_h = 75^o$, $\theta_p = 130^o$, $k_1 = k_3 = 100$, $R_0 = 0.1L$.

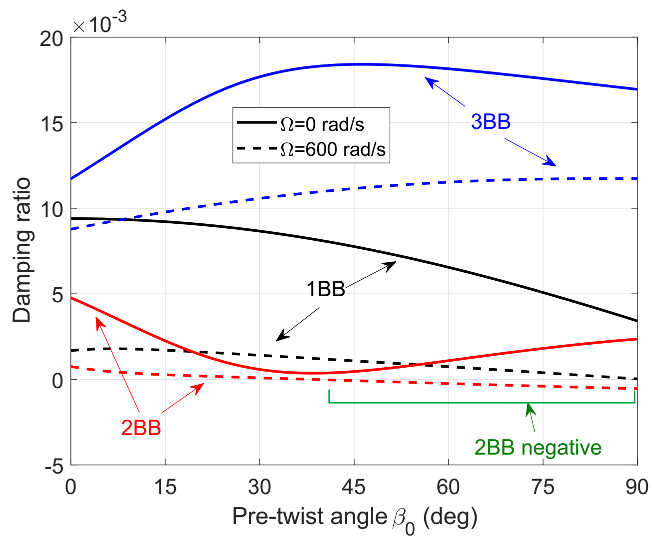

Figure 30: Damping ratios of the first three modes of BB-subsystem vs. pretwist angle β_0 for selected rotating speeds Ω; $\theta_h = 75^o$, $\theta_p = 130^o$, $k_1 = k_3 = 100$, $R_0 = 0.1L$.

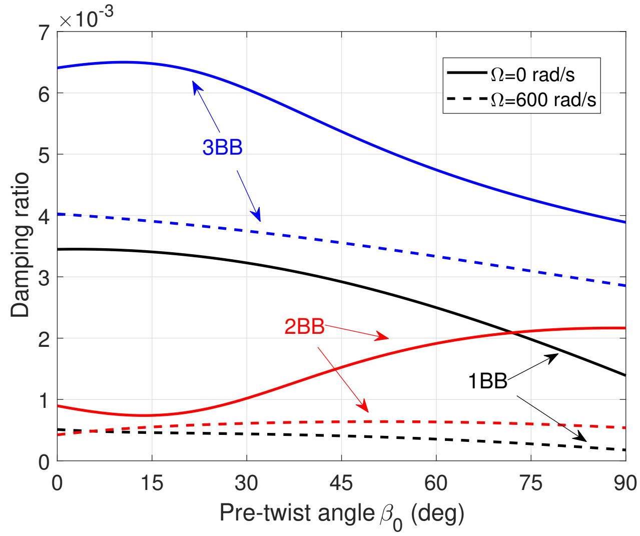

Figure 31: Damping ratios of the first three modes of BB-subsystem vs. pretwist angle β_0 for selected rotating speeds Ω; $\theta_h = 75^o$, $\theta_p = 90^o$, $k_1 = k_3 = 100$, $R_0 = 0.1L$.

8.5.2. TE-subsystem

The influence of pretwist angle β_0 on frequencies and damping ratios of the twist modes are illustrated in Figs. 32 and 33, respectively. It can be seen the influences of β_0 are negligible both in Figs. 32 and 33.

9. Conclusions

A fiber-reinforced composite rotary thin-walled beam theory incorporating piezo-composite actuators is developed. The circumferentially uniform stiffness (CUS) lay-up configuration is adopted to decouple the system into two independent subsystems, viz., flapping-lagging coupled BB-subsystem and twist-extension coupled TE-subsystem. Based on a simple negative velocity feedback control algorithm, the relationships between control authority and piezo-actuator, host structure elastic tailoring, rotating speed, presetting and pretwist angles are investigated. As shown in Figs. 14 and 15, piezoelectric transverse shear force (in dashed lines) and bending moment (in solid lines) have the better

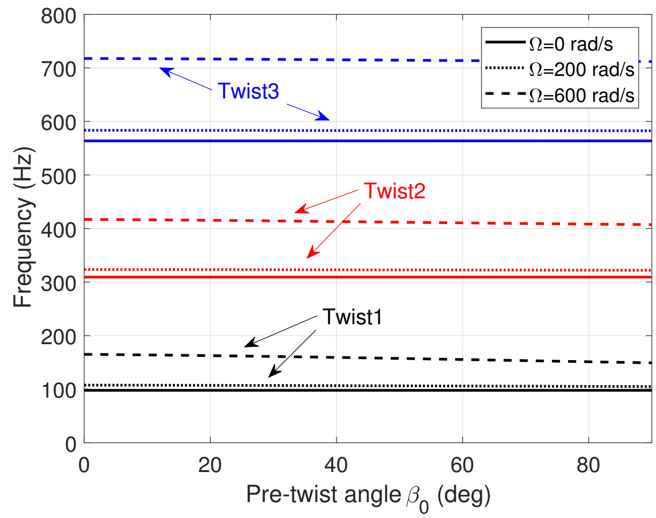

Figure 32: Frequencies of TE-subsystem vs. pretwist angle β_0 for selected rotating speeds Ω; $\theta_h = 75^o$, $\theta_p = 130^o$, $k_2 = k_4 = 10$, $R_0 = 0.1L$.

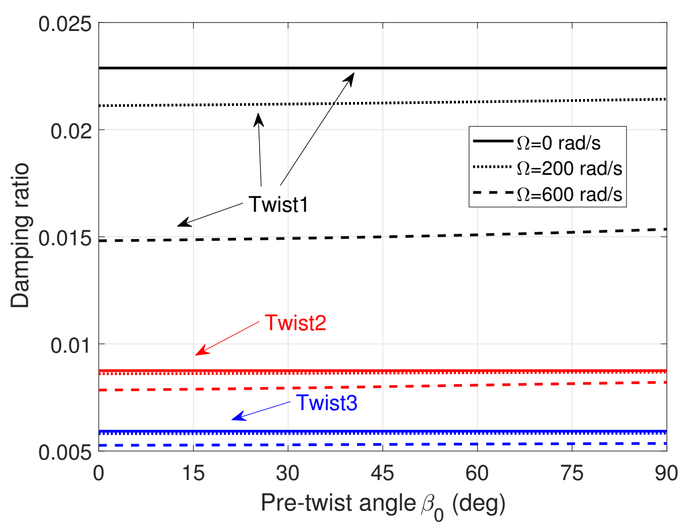

Figure 33: Damping ratios of TE-subsystem vs. pretwist angle β_0 for selected rotating speeds Ω, $\theta_h = 75^o$, $\theta_p = 130^o$, $k_2 = k_4 = 10$, $R_0 = 0.1L$.

control authority on strong and weak bending-bending elastic coupling cases, respectively. Actually for the strong elastic coupling ($\theta_h = 75^o$) case, damping ratios induced by piezoelectric transverse shear force are over twice those induced by piezoelectric bending moment. The design factors, such as rotating speed (see Figs. 21 and 23), presetting angle (see Fig. 24) and pretwist angle (see Figs. 30 and 31), all have significant effects on control authority of BB-subsystem. However, the results of Figs. 26, 28 and 33 make clear that these factors influence significantly only the fundamental twist mode of TE-subsystem.

Appendix A. 1-D inertial coefficients b_{ij}

$$b_1 = b_1^p, \quad b_{10} = b_{10}^p, \tag{A.1}$$

$$b_4 = b_4^p \cos^2\beta + b_5^p \sin^2\beta - 2b_6^p \sin\beta\cos\beta, \tag{A.2}$$

$$b_5 = b_5^p \cos^2\beta + b_4^p \sin^2\beta + 2b_6^p \sin\beta\cos\beta, \tag{A.3}$$

$$b_6 = b_6^p(\cos^2\beta - \sin^2\beta) + (b_4^p - b_5^p)\sin\beta\cos\beta, \tag{A.4}$$

in which

$$(b_1^p,\ b_4^p,\ b_5^p,\ b_6^p,\ b_{10}^p) = \oint_c \left(1,\ z^2,\ x^2,\ xz,\ {F_w}^2\right) \left[\sum_{k=1}^{N_{hp}} \int_{n_{k1}}^{n_{k2}} \rho_{(k)}\,\mathrm{d}\,n\right] \mathrm{d}\,s. \tag{A.5}$$

Appendix B. Global stiffness quantities a_{ij}

$$a_{11} = a_{11}^p, \quad a_{16} = a_{16}^p, \quad a_{17} = a_{17}^p, \quad a_{18} = a_{18}^p, \tag{B.1a}$$

$$a_{28} = a_{28}^p, \quad a_{66} = a_{66}^p, \quad a_{67} = a_{67}^p, \quad a_{68} = a_{68}^p, \tag{B.1b}$$

$$a_{77} = a_{77}^p, \quad a_{78} = a_{78}^p, \quad a_{88} = a_{88}^p. \tag{B.1c}$$

$$a_{12} = a_{12}^p\cos\beta + a_{13}^p\sin\beta, \quad a_{13} = a_{13}^P\cos\beta - a_{12}^p\sin\beta, \tag{B.2}$$

$$a_{14} = a_{14}^p\cos\beta + a_{15}^p\sin\beta, \quad a_{15} = a_{15}^p\cos\beta - a_{14}^p\sin\beta, \tag{B.3}$$

$$a_{26} = a_{26}^p\cos\beta + a_{36}^p\sin\beta, \quad a_{27} = a_{27}^p\cos\beta + a_{37}^p\sin\beta, \tag{B.4}$$

$$a_{36} = a_{36}^p\cos\beta - a_{26}^p\sin\beta, \quad a_{37} = a_{37}^p\cos\beta - a_{27}^p\sin\beta, \tag{B.5}$$

$$a_{38} = a_{38}^p\cos\beta - a_{28}^p\sin\beta, \quad a_{46} = a_{46}^p\cos\beta + a_{56}^p\sin\beta, \tag{B.6}$$

$$a_{47} = a_{47}^p\cos\beta + a_{57}^p\sin\beta, \quad a_{48} = a_{48}^p\cos\beta + a_{58}^p\sin\beta, \tag{B.7}$$

$$a_{56} = a_{56}^p\cos\beta - a_{46}^p\sin\beta, \quad a_{57} = a_{57}^p\cos\beta - a_{47}^p\sin\beta, \tag{B.8}$$

$$a_{58} = a_{58}^p\cos\beta - a_{48}^p\sin\beta. \tag{B.9}$$

$$a_{22} = a_{22}^p \cos^2\beta + a_{33}^p \sin^2\beta + 2a_{23}^p \cos\beta\sin\beta, \tag{B.10}$$

$$a_{23} = a_{23}^p(\cos^2\beta - \sin^2\beta) + (a_{33}^p - a_{22}^p)\cos\beta\sin\beta, \tag{B.11}$$

$$a_{24} = a_{24}^p \cos^2\beta + a_{35}^p \sin^2\beta + (a_{25}^p + a_{34}^p)\cos\beta\sin\beta, \tag{B.12}$$

$$a_{25} = a_{25}^p \cos^2\beta - a_{34}^p \sin^2\beta + (a_{35}^p - a_{24}^p)\cos\beta\sin\beta, \tag{B.13}$$

$$a_{33} = a_{33}^p \cos^2\beta + a_{22}^p \sin^2\beta - 2a_{23}^p \cos\beta\sin\beta, \tag{B.14}$$

$$a_{34} = a_{34}^p \cos^2\beta - a_{25}^p \sin^2\beta + (a_{35}^p - a_{24}^p)\cos\beta\sin\beta, \tag{B.15}$$

$$a_{35} = a_{35}^P \cos^2\beta + a_{24}^p \sin^2\beta - (a_{34}^p + a_{25}^p)\cos\beta\sin\beta, \tag{B.16}$$

$$a_{44} = a_{44}^p \cos^2\beta + a_{55}^p \sin^2\beta + 2a_{45}^p \cos\beta\sin\beta, \tag{B.17}$$

$$a_{45} = a_{45}^p(\cos^2\beta - \sin^2\beta) + (a_{55}^p - a_{44}^p)\cos\beta\sin\beta, \tag{B.18}$$

$$a_{55} = a_{55}^p \cos^2\beta + a_{44}^p \sin^2\beta - 2a_{45}^p \cos\beta\sin\beta. \tag{B.19}$$

Note that, the definitions of local stiffness quantities a_{ij}^p are given in the Appendix of Ref. [29].

Appendix C. The piezo-actuator coefficients $\mathcal{A}_i^X$

The subscript $i = 1, 2, 3, 4$ of piezo-actuator coefficients $\mathcal{A}_i^X$ denote the operation

$$\mathcal{A}_1^X = \int_T \mathcal{A}_T^X \,\mathrm{d}\,s - \int_B \mathcal{A}_B^X \,\mathrm{d}\,s, \quad \mathcal{A}_2^X = \int_T \mathcal{A}_T^X \,\mathrm{d}\,s + \int_B \mathcal{A}_B^X \,\mathrm{d}\,s, \tag{C.1a}$$

$$\mathcal{A}_3^X = \int_L \mathcal{A}_L^X \,\mathrm{d}\,s - \int_R \mathcal{A}_R^X \,\mathrm{d}\,s, \quad \mathcal{A}_4^X = \int_L \mathcal{A}_L^X \,\mathrm{d}\,s + \int_R \mathcal{A}_R^X \,\mathrm{d}\,s, \tag{C.1b}$$

where T, B, L and R denote top, bottom, left and right wall, respectively. And $\mathcal{A}^X$ are given as

$$\mathcal{A}^{Ty} = \sum_{k=1}^{N_p} \left(e_{yy} - \frac{A_{12}}{A_{11}} e_{ss} \right) \frac{(n_{k2} - n_{k1})}{\hat{h}} P_k(s), \tag{C.2a}$$

$$\begin{aligned}\mathcal{A}^{Mz} = \sum_{k=1}^{N_p} \Bigg\{ & x \left(e_{yy} - \frac{A_{12}}{A_{11}} e_{ss} \right) \frac{(n_{k2} - n_{k1})}{\hat{h}} P_k(s) \\ & - \frac{\mathrm{d}\,z}{\mathrm{d}\,s} \left[\frac{1}{2} e_{yy}(n_{k1} + n_{k2}) - \frac{B_{12}}{A_{11}} e_{ss} \right] \frac{(n_{k2} - n_{k1})}{\hat{h}} P_k(s) \Bigg\},\end{aligned} \tag{C.2b}$$

$$
\begin{aligned}
\mathcal{A}^{Mx} &= \sum_{k=1}^{N_p} \Big\{ z \left(e_{yy} - \frac{A_{12}}{A_{11}} e_{ss} \right) \frac{(n_{k2} - n_{k1})}{\hat{h}} P_k(s) \\
&+ \frac{\mathrm{d}\,x}{\mathrm{d}\,s} \left[\frac{1}{2} e_{yy} (n_{k1} + n_{k2}) - \frac{B_{12}}{A_{11}} e_{ss} \right] \frac{(n_{k2} - n_{k1})}{\hat{h}} P_k(s) \Big\},
\end{aligned} \tag{C.2c}
$$

$$
\mathcal{A}^{Qx} = \sum_{k=1}^{N_p} \frac{\mathrm{d}\,x}{\mathrm{d}\,s} \left(e_{sy} - \frac{A_{16}}{A_{11}} e_{ss} \right) \frac{(n_{k2} - n_{k1})}{\hat{h}} P_k(s), \tag{C.2d}
$$

$$
\mathcal{A}^{Qz} = \sum_{k=1}^{N_p} \frac{\mathrm{d}\,z}{\mathrm{d}\,s} \left(e_{sy} - \frac{A_{16}}{A_{11}} e_{ss} \right) \frac{(n_{k2} - n_{k1})}{\hat{h}} P_k(s), \tag{C.2e}
$$

$$
\begin{aligned}
\mathcal{A}^{Bw} &= - \sum_{k=1}^{N_p} \Big\{ F_w \left(e_{yy} - \frac{A_{12}}{A_{11}} e_{ss} \right) \frac{(n_{k2} - n_{k1})}{\hat{h}} P_k(s) \\
&+ a(s) \left[\frac{1}{2} e_{yy} (n_{k1} + n_{k2}) - \frac{B_{12}}{A_{11}} e_{ss} \right] \frac{(n_{k2} - n_{k1})}{\hat{h}} P_k(s) \Big\},
\end{aligned} \tag{C.2f}
$$

$$
\begin{aligned}
\mathcal{A}^{My} &= \sum_{k=1}^{N_p} \Big\{ \psi(s) \left(e_{sy} - \frac{A_{16}}{A_{11}} e_{ss} \right) \frac{(n_{k2} - n_{k1})}{\hat{h}} P_k(s) \\
&+ 2 \left[\frac{1}{2} e_{sy} (n_{k1} + n_{k2}) - \frac{B_{16}}{A_{11}} e_{ss} \right] \frac{(n_{k2} - n_{k1})}{\hat{h}} P_k(s) \Big\},
\end{aligned} \tag{C.2g}
$$

$$
\begin{aligned}
\mathcal{A}^{\Gamma t} &= \sum_{k=1}^{N_p} \Big\{ (x^2 + z^2) \left(e_{yy} - \frac{A_{12}}{A_{11}} e_{ss} \right) \frac{(n_{k2} - n_{k1})}{\hat{h}} P_k(s) \\
&+ 2 r_n \left[\frac{1}{2} e_{yy} (n_{k1} + n_{k2}) - \frac{B_{12}}{A_{11}} e_{ss} \right] \frac{(n_{k2} - n_{k1})}{\hat{h}} P_k(s) \Big\}.
\end{aligned} \tag{C.2h}
$$

Appendix D. Matrix via the Extended Galerkin's Method

Mass matrix

$$
\mathbf{M}_B = \int_0^L \begin{bmatrix} b_1 \boldsymbol{\Psi}_u \boldsymbol{\Psi}_u^T & 0 & 0 & 0 \\ 0 & b_1 \boldsymbol{\Psi}_w \boldsymbol{\Psi}_w^T & 0 & 0 \\ 0 & 0 & b_4 \boldsymbol{\Psi}_x \boldsymbol{\Psi}_x^T & b_6 \boldsymbol{\Psi}_x \boldsymbol{\Psi}_z^T \\ 0 & 0 & b_6 \boldsymbol{\Psi}_z \boldsymbol{\Psi}_x^T & b_5 \boldsymbol{\Psi}_z \boldsymbol{\Psi}_z^T \end{bmatrix} \mathrm{d}\,y. \tag{D.1}
$$

$$\mathbf{M}_T = \int_0^L \begin{bmatrix} b_1 \boldsymbol{\Psi}_v \boldsymbol{\Psi}_v^T & 0 \\ 0 & (b_4+b_5)\boldsymbol{\Psi}_\phi \boldsymbol{\Psi}_\phi^T + b_{10} \boldsymbol{\Psi'}_\phi \boldsymbol{\Psi'}_\phi^T \end{bmatrix} \mathrm{d}\, y. \tag{D.2}$$

Stiffness matrix

$$\mathbf{K}_B = \int_0^L \begin{bmatrix} a_{44} \boldsymbol{\Psi}'_u \boldsymbol{\Psi}'_u{}^T & a_{45} \boldsymbol{\Psi}'_u \boldsymbol{\Psi}'_w{}^T & a_{34} \boldsymbol{\Psi}'_u \boldsymbol{\Psi}'_x{}^T + a_{45} \boldsymbol{\Psi}'_u \boldsymbol{\Psi}_x{}^T & a_{24} \boldsymbol{\Psi}'_u \boldsymbol{\Psi}'_z{}^T + a_{44} \boldsymbol{\Psi}'_u \boldsymbol{\Psi}_z{}^T \\ & a_{55} \boldsymbol{\Psi}'_w \boldsymbol{\Psi}'_w{}^T & a_{35} \boldsymbol{\Psi}'_w \boldsymbol{\Psi}'_x{}^T + a_{55} \boldsymbol{\Psi}'_w \boldsymbol{\Psi}_x{}^T & a_{25} \boldsymbol{\Psi}'_w \boldsymbol{\Psi}'_z{}^T + a_{45} \boldsymbol{\Psi}'_w \boldsymbol{\Psi}_z{}^T \\ & & \mathbf{K}_{55} & \mathbf{K}_{56} \\ \text{Symm} & & & \mathbf{K}_{66} \end{bmatrix} \mathrm{d}\, y, \tag{D.3}$$

with

$$\begin{cases} \mathbf{K}_{55} = a_{33} \boldsymbol{\Psi}'_x \boldsymbol{\Psi}'_x{}^T + a_{35} \boldsymbol{\Psi}'_x \boldsymbol{\Psi}_x{}^T + a_{35} \boldsymbol{\Psi}_x \boldsymbol{\Psi}'_x{}^T + a_{55} \boldsymbol{\Psi}_x \boldsymbol{\Psi}_x{}^T, \\ \mathbf{K}_{56} = a_{23} \boldsymbol{\Psi}'_x \boldsymbol{\Psi}'_z{}^T + a_{34} \boldsymbol{\Psi}'_x \boldsymbol{\Psi}_z{}^T + a_{25} \boldsymbol{\Psi}_x \boldsymbol{\Psi}'_z{}^T + a_{45} \boldsymbol{\Psi}_x \boldsymbol{\Psi}_z{}^T, \\ \mathbf{K}_{66} = a_{22} \boldsymbol{\Psi}'_z \boldsymbol{\Psi}'_z{}^T + a_{24} \boldsymbol{\Psi}'_z \boldsymbol{\Psi}_z{}^T + a_{24} \boldsymbol{\Psi}_z \boldsymbol{\Psi}'_z{}^T + a_{44} \boldsymbol{\Psi}_z \boldsymbol{\Psi}_z{}^T. \end{cases} \tag{D.4}$$

$$\mathbf{K}_T = \int_0^L \begin{bmatrix} a_{11} \boldsymbol{\Psi}'_v \boldsymbol{\Psi}'_v{}^T & a_{17} \boldsymbol{\Psi}'_v \boldsymbol{\Psi}'_\phi{}^T \\ a_{17} \boldsymbol{\Psi}'_\phi \boldsymbol{\Psi}'_v{}^T & a_{77} \boldsymbol{\Psi}'_\phi \boldsymbol{\Psi}'_\phi{}^T + a_{66} \boldsymbol{\Psi}''_\phi \boldsymbol{\Psi}''^T_\phi \end{bmatrix} \mathrm{d}\, y. \tag{D.5}$$

Additional stiffness matrix

$$\hat{\mathbf{K}}_B = \int_0^L \begin{bmatrix} b_1 R(y) \boldsymbol{\Psi}'_u \boldsymbol{\Psi}'_u{}^T - b_1 \boldsymbol{\Psi}_u \boldsymbol{\Psi}_u{}^T & 0 & 0 & 0 \\ 0 & b_1 R(y) \boldsymbol{\Psi}'_w \boldsymbol{\Psi}'_w{}^T & 0 & 0 \\ 0 & 0 & -b_4 \boldsymbol{\Psi}_x \boldsymbol{\Psi}_x{}^T & -b_6 \boldsymbol{\Psi}_x \boldsymbol{\Psi}_z{}^T \\ 0 & 0 & -b_6 \boldsymbol{\Psi}_z \boldsymbol{\Psi}_x{}^T & -b_5 \boldsymbol{\Psi}_z \boldsymbol{\Psi}_z{}^T \end{bmatrix} \mathrm{d}\, y, \tag{D.6}$$

$$\hat{\mathbf{K}}_T = \int_0^L \begin{bmatrix} -b_1 \boldsymbol{\Psi}_v \boldsymbol{\Psi}_v{}^T & 0 \\ 0 & -(b_4 - b_5 - b_6) \boldsymbol{\Psi}_\phi \boldsymbol{\Psi}_\phi{}^T + (b_4+b_5) R(y) \boldsymbol{\Psi}'_\phi \boldsymbol{\Psi}'_\phi{}^T - b_{10} \boldsymbol{\Psi}'_\phi \boldsymbol{\Psi}'_\phi{}^T \end{bmatrix} \mathrm{d}\, y. \tag{D.7}$$

Actuating matrix

$$\mathcal{A}_B = \int_0^L \begin{bmatrix} \mathcal{A}_1^{Qx} \boldsymbol{\Psi}'_u \cos\beta & \mathcal{A}_3^{Qz} \boldsymbol{\Psi}'_u \sin\beta \\ -\mathcal{A}_1^{Qx} \boldsymbol{\Psi}'_u \sin\beta & \mathcal{A}_3^{Qz} \boldsymbol{\Psi}'_w \cos\beta \\ \mathcal{A}_1^{Mx} \boldsymbol{\Psi}'_x \cos\beta - \mathcal{A}_1^{Qx} \boldsymbol{\Psi}_x \sin\beta & -\mathcal{A}_3^{Mz} \boldsymbol{\Psi}'_x \sin\beta + \mathcal{A}_3^{Qz} \boldsymbol{\Psi}_x \cos\beta \\ \mathcal{A}_1^{Mx} \boldsymbol{\Psi}'_z \sin\beta + \mathcal{A}_1^{Qx} \boldsymbol{\Psi}_z \cos\beta & \mathcal{A}_3^{Mz} \boldsymbol{\Psi}'_z \cos\beta + \mathcal{A}_3^{Qz} \boldsymbol{\Psi}_x \sin\beta \end{bmatrix} P(y)\, \mathrm{d}\, y. \tag{D.8}$$

$$\mathcal{A}_T = \int_0^L \begin{bmatrix} \mathcal{A}_2^{Ty} \boldsymbol{\Psi}'_v & \mathcal{A}_4^{Ty} \boldsymbol{\Psi}'_v \\ \mathcal{A}_2^{My} \boldsymbol{\Psi}'_\phi & \mathcal{A}_4^{My} \boldsymbol{\Psi}'_\phi \end{bmatrix} P(y) \,\mathrm{d}\, y. \tag{D.9}$$

External forces vector

$$\mathbf{Q}_B = \begin{Bmatrix} \int_0^L p_x \boldsymbol{\Psi}_u \,\mathrm{d}\, y + \bar{Q}_x \boldsymbol{\Psi}_u(L) \\ \int_0^L p_z \boldsymbol{\Psi}_w \,\mathrm{d}\, y + \bar{Q}_z \boldsymbol{\Psi}_w(L) \\ \int_0^L m_x \boldsymbol{\Psi}_x \,\mathrm{d}\, y + \bar{M}_x \boldsymbol{\Psi}_x(L) \\ \int_0^L m_z \boldsymbol{\Psi}_z \,\mathrm{d}\, y + \bar{M}_z \boldsymbol{\Psi}_z(L) \end{Bmatrix}. \tag{D.10}$$

$$\mathbf{Q}_T = \begin{Bmatrix} \int_0^L [\Omega^2 (R_0 + y) + p_y] \boldsymbol{\Psi}_v \,\mathrm{d}\, y + \bar{T}_y \boldsymbol{\Psi}_v(L) \\ \int_0^L (\Omega^2 b_6 + m_y + b'_w) \boldsymbol{\Psi}_\phi \,\mathrm{d}\, y + [\bar{M}_y \boldsymbol{\Psi}_\phi(L) + \bar{B}_w \boldsymbol{\Psi}'_\phi(L)] \end{Bmatrix}. \tag{D.11}$$

Control matrix

$$\mathbf{P}_B = \begin{bmatrix} 0 & 0 & k_1 \cos\beta(Y_s) {\boldsymbol{\Psi}_x}^T(Y_s) & k_1 \sin\beta(Y_s) {\boldsymbol{\Psi}_z}^T(Y_s) \\ 0 & 0 & k_3 \sin\beta(Y_s) {\boldsymbol{\Psi}_x}^T(Y_s) & -k_3 \cos\beta(Y_s) {\boldsymbol{\Psi}_z}^T(Y_s) \end{bmatrix}, \tag{D.12}$$

$$\mathbf{P}_T = \begin{bmatrix} 0 & -k_2 {\boldsymbol{\Psi}_\phi}^T(Y_s) \\ 0 & -k_4 {\boldsymbol{\Psi}_\phi}^T(Y_s) \end{bmatrix}. \tag{D.13}$$

References

[1] D. H. Hodges, Review of composite rotor blade modeling, AIAA journal 28 (3) (1990) 561–565.

[2] O. Rand, Analysis of composite rotor blades, in: Numerical Analysis and Modelling of Composite Materials, Springer, 1996, pp. 1–26.

[3] S. N. Jung, V. Nagaraj, I. Chopra, Refined structural dynamics model for composite rotor blades, AIAA journal 39 (2) (2001) 339–348.

[4] E. Carrera, M. Filippi, E. Zappino, Free vibration analysis of rotating composite blades via carrera unified formulation, Composite Structures 106 (2013) 317–325.

[5] F. Demoures, F. Gay-Balmaz, S. Leyendecker, S. Ober-Blöbaum, T. S. Ratiu, Y. Weinand, Discrete variational lie group formulation of geometrically exact beam dynamics, Numerische Mathematik 130 (1) (2015) 73–123. doi:10.1007/s00211-014-0659-4.
URL http://dx.doi.org/10.1007/s00211-014-0659-4

[6] L. W. Rehfield, A. R. Atilgan, D. H. Hodges, Nonclassical behavior of thin-walled composite beams with closed cross sections, Journal of the American Helicopter Society 35 (2) (1990) 42–50.

[7] R. Chandra, I. Chopra, Experimental-theoretical investigation of the vibration characteristics of rotating composite box beams, Journal of Aircraft 29 (4) (1992) 657–664.

[8] O. Song, L. Librescu, Structural modeling and free vibration analysis of rotating composite thin-walled beams, Journal of the American Helicopter Society 42 (4) (1997) 358–369.

[9] O. Song, N.-H. Jeong, L. Librescu, Vibration and stability of pretwisted spinning thin-walled composite beams featuring bending–bending elastic coupling, Journal of Sound and Vibration 237 (3) (2000) 513–533.

[10] S.-Y. Oh, O. Song, L. Librescu, Effects of pretwist and presetting on coupled bending vibrations of rotating thin-walled composite beams, Int. J. Solids Struct. 40 (5) (2003) 1203–1224.

[11] S.-Y. Oh, L. Librescu, O. Song, Modelling and vibration of composite thin-walled rotating blades featuring extension-twist elastic coupling, Aeronautical Journal 109 (1095) (2005) 233–246.

[12] G. L. Ghiringhelli, P. Masarati, M. Morandini, D. Muffo, Integrated aeroservoelastic analysis of induced strain rotor blades, Mechanics of Advanced Materials and Structures 15 (3-4) (2008) 291–306.

[13] C. Brillante, M. Morandini, P. Mantegazza, Periodic controllers for vibration reduction using actively twisted blades, The Aeronautical Journal 120 (1233) (2016) 1763–1784. `doi:10.1017/aer.2016.80`.
URL `https://www.cambridge.org/core/journals/aeronautical-journal/article/div-classtitleperiodic-controllers-for-vibration-reduction-using-actively-twisted-blade 89330CE640F7C750DE4FF561D31DF3D4`

[14] S. Glukhikh, E. Barkanov, A. Kovalev, P. Masarati, M. Morandini, J. Riemenschneider, P. Wierach, Design of helicopter rotor blades with actuators made of a piezomacrofiber composite, Mechanics of Composite Materials 44 (1) (2008) 57–64.

[15] G. L. Ghiringhelli, P. Masarati, P. Mantegazza, Characterisation of anisotropic, non-homogeneous beam sections with embedded piezo-electric materials, Journal of Intelligent Material Systems and Structures 8 (10) (1997) 842–858.

[16] P. Masarati, G. L. Ghiringhelli, Characterization of anisotropic, non-homogeneous plates with piezoelectric inclusions, Computers & Structures 83 (15-16) (2005) 1171–1190. `doi:doi:DOI:10.1016/j.compstruc.2004.10.017`.

URL http://www.sciencedirect.com/science/article/B6V28-4FKY8WG-1/2/c4da0f3cbc7e9cbd655e84b284c805c8

[17] A. A. Bent, Active fiber composites for structural actuation, Ph.D. thesis, Massachusetts Institute of Technology (1997).

[18] W. K. Wilkie, R. G. Bryant, J. W. High, R. L. Fox, R. F. Hellbaum, A. Jalink Jr, B. D. Little, P. H. Mirick, Low-cost piezocomposite actuator for structural control applications, in: SPIE's 7th Annual International Symposium on Smart Structures and Materials, International Society for Optics and Photonics, 2000, pp. 323–334.

[19] L. Librescu, S. S. Na, Dynamic response of cantilevered thin-walled beams to blast and sonic-boom loadings, Shock and Vibration 5 (1) (1998) 23–33.

[20] S. Na, L. Librescu, Oscillation control of cantilevers via smart materials technology and optimal feedback control: actuator location and power consumption issues, Smart Materials and Structures 7 (6) (1998) 833.

[21] S. Na, L. Librescu, M.-H. Kim, I.-J. Jeong, P. Marzocca, Robust aeroelastic control of flapped wing systems using a sliding mode observer, Aerosp. Sci. Technol. 10 (2) (2006) 120–126.

[22] S.-C. Choi, J.-S. Park, J.-H. Kim, Vibration control of pre-twisted rotating composite thin-walled beams with piezoelectric fiber composites, J. Sound Vib. 300 (1) (2007) 176–196.

[23] L. Librescu, S. Na, Z. Qin, B. Lee, Active aeroelastic control of aircraft composite wings impacted by explosive blasts, J. Sound Vib. 318 (1) (2008) 74–92.

[24] S.-J. Cha, J.-S. Song, H.-H. Lee, S. Na, J.-H. Shim, P. Marzocca, Dynamic response control of rotating thin-walled composite blade exposed to external excitations, J. Aerosp. Eng. 27 (5) (2014) 04014025.

[25] R. Kielb, Effects of warping and pretwist on torsional vibration of rotating beams, Journal of applied mechanics 51 (1984) 913.

[26] L. W. Rehfield, A. R. Atilgan, Shear center and elastic axis and their usefulness for composite thin-walled beams, in: Technical Conference on Composite Materials, 1989, pp. 179–188.

[27] R. C. Lake, M. W. Nixon, M. L. Wilbur, J. D. Singleton, R. Mirick, A demonstration of passive blade twist control using extension-twist coupling, in: Proceedings of the SDM Conference, Dallas, TX, April, 1992, pp. 13–15.

[28] S. Ozbay, O. Bauchau, D. S. Dancila, E. A. Armanios, Extension-twist coupling optimization in composite rotor blades, in: Proceedings of the 46th AIAA/ASME/ASCE/AHS/ASC Structures, Structural Dynamics and Materials Conference, 2005, pp. 18–21.

[29] X. Wang, Z. Qin, Nonlinear modal interactions in composite thin-walled beam structures with simultaneous 1:2 internal and 1:1 external resonances, Nonlinear Dynamics 86 (2) (2016) 1381–1405. doi:10.1007/s11071-016-2970-3.
URL http://dx.doi.org/10.1007/s11071-016-2970-3

[30] R. M. Jones, Mechanics of composite materials, CRC press, 1998.

[31] L. Librescu, O. Song, Thin-Walled Composite Beams: Theory and Application, Springer, New York, 2006, chap.8, pp. 213-232.

[32] X. Wang, M. Morandini, P. Masarati, Velocity feedback damping of piezo-actuated wings, Composite Structures 174 (2017) 221 – 232. doi:https://doi.org/10.1016/j.compstruct.2017.04.016.
URL http://www.sciencedirect.com/science/article/pii/S0263822317304233

[33] Z. Qin, L. Librescu, On a shear-deformable theory of anisotropic thin-walled beams: further contribution and validation, Compos. Struct. 56 (4) (2002) 345–358.

[34] L. W. Rehfield, A. R. Atilgan, Toward understanding the tailoring mechanisms for thin-walled composite tubular beams, in: Proceedings of the First USSR-US Symposium on Mechanics of Composite Materials, Riga, Latvia, May, 1989, pp. 23–26.

[35] D. Ewins, R. Henry, Structural dynamic characteristics of individual blades, Lecture series-van Kareman Institute for fluid dynamics 6 (1992) B1–B28.

[36] L. Librescu, S. Na, Dyanmic response of cantilevered thin-wlled beams to blast and sonic-boom loadings, Shock. Vib. 5 (1) (1998) 23–33.

[37] A. Palazotto, P. Linnemann, Vibration and buckling characteristics of composite cylindrical panels incorporating the effects of a higher order shear theory, Int. J. Solids Struct. 28 (3) (1991) 341–361.

[38] L. Librescu, L. Meirovitch, S. S. Na, Control of cantilever vibration via structural tailoring and adaptive materials, AIAA journal 35 (8) (1997) 1309–1315.

[39] S. Na, L. Librescu, J. K. Shim, Modeling and bending vibration control of nonuniform thin-walled rotating beams incorporating adaptive capabilities, International Journal of Mechanical Sciences 45 (8) (2003) 1347–1367.

[40] A. D. Stemple, S. W. Lee, A finite element model for composite beams undergoing large deflection with arbitrary cross-sectional warping, Int. J. Numer. Methods Eng. 28 (9) (1989) 2143–2160.

[41] A. J. Du Plessis, Modeling and experimental testing of twist actuated single cell composite beams for helicopter blade control, Ph.D. thesis, Massachusetts Institute of Technology (1996).

[42] J.-S. Park, J.-H. Kim, Analytical development of single crystal macro fiber composite actuators for active twist rotor blades, Smart Mater. Struct. 14 (4) (2005) 745.

List of Figures

List of Tables